








Simulations of surface acoustic wave interactions on a sessile droplet using a three-dimensional multiphase lattice Boltzmann model

Stephen B. Burnside ¹, Kamil Pasieczynski ¹, Amin Zarareh ¹, Mubbashar Mehmood ¹,
Yong Qing Fu ² and Baixin Chen ^{1,*}

¹*Institute of Mechanical, Process and Energy Engineering, Heriot-Watt University, Edinburgh EH14 4AS, United Kingdom*

²*Faculty of Engineering and Environment, Northumbria University, Newcastle upon Tyne, NE1 8ST, United Kingdom*

 (Received 8 October 2020; revised 12 February 2021; accepted 8 September 2021; published 1 October 2021)

This study reports the development of a three-dimensional numerical model for acoustic interactions with a microscale sessile droplet under surface acoustic wave (SAW) excitation using the lattice Boltzmann method (LBM). We first validate the model before SAW interactions are added. The results demonstrate good agreement with the analytical results for thermodynamic consistency, Laplace law, static contact angle on a flat surface, and droplet oscillation. We then investigate SAW interactions on the droplet, with resonant frequencies ranging 61.7–250.1 MHz. According to our findings, an increase in wave amplitude elicits an increase in streaming velocity inside the droplet, causing internal mixing, and further increase in wave amplitude leads to pumping and jetting. The boundaries of wave amplitude at various resonant frequencies are predicted for mixing, pumping, and jetting modes. The modeling predictions on the roles of forces (SAW, interfacial tension, inertia, and viscosity) on the dynamics of mixing, pumping, and jetting of a droplet are in good agreement with observations and experimental data. The model is further applied to investigate the effects of SAW substrate surface wettability, viscosity ratio, and interfacial tension on SAW actuation onto the droplet. This work demonstrates the capability of the LBM in the investigation of acoustic wave interactions between SAW and a liquid medium.

DOI: [10.1103/PhysRevE.104.045301](https://doi.org/10.1103/PhysRevE.104.045301)

I. INTRODUCTION

Over the past few years, there has been a move towards integrating complete laboratory chemical analysis procedures onto the surface of a microfluidic chip, known as lab on a chip (LOC) [1–3]. Unfortunately, when scaling the processes down to the microscale, there are some technical problems, such as the pumping of fluids becomes increasingly more difficult as viscous and capillary forces become more dominant. Additionally, mixing of chemical or biological materials at a small scale can be inefficient and tedious due to the large time and length scales required.

Recently, surface acoustic waves (SAWs) have been shown to demonstrate features that could have positive implications for the development of microfluidic devices [4]. SAWs can be initiated by manipulating the frequency of the interdigital transducer (IDT) on the surface of a piezoelectric substrate. When a liquid medium lies in the path of the propagating SAW, the wave changes mode as it penetrates the boundary between the liquid and SAW substrate. The attenuation of the leaky SAW (LSAW) generates significant acoustic streaming inside the fluid, which enables pumping, mixing, jetting, and nebulization to occur [5]. These phenomena can be exploited in the diagnosis of diseases, DNA sorting, and drug delivery systems [6–8] in addition to applications including cleaning, among several others [9].

To date, there have been a small number of studies modeling the interaction between the SAW and a droplet. Alghane and co-workers [10,11] used a finite volume (FV) scheme to investigate three-dimensional (3D) acoustic streaming within microdroplets. They concluded that the maximum streaming velocity is achieved when the width of the SAW is approximately half the droplet radius. The authors also reported strong nonlinearity in the flow inertia, suggesting the Stokes model is only valid for very small acoustic powers [12]. It should be noted that in their numerical scheme the droplet is assumed to have a rigid boundary, neglecting deformations of droplet. Riaud *et al.* [13] investigated the influence of viscosity and caustics on acoustic streaming in droplets both experimentally and numerically. The findings from the study suggest that viscosity influences the flow structure as well as the velocity magnitude, whereas caustics appear to drive the flow. Köster [14] conducted a comprehensive study investigating acoustic streaming on biochips. The author briefly describes a method to capture surface deformation in sessile drops which preserves the volume, however this is a very restricted study, consisting of only one special case. Recently, the lattice Boltzmann (LB) methodology has been used in the study of acoustic streaming and attenuation-driven acoustic streaming. Tan and Yeo [15], studied acoustic streaming in micro- and nanochannels under SAW excitation by means of a hybrid numerical scheme comprised of the finite-difference (FD) technique for elastic solid and the LB method for fluid flows. The findings show good agreement with the analytical solutions, demonstrating a viability of using the LB in the exploration of SAW effects on liquids. More recently,

*b.chen@hw.ac.uk

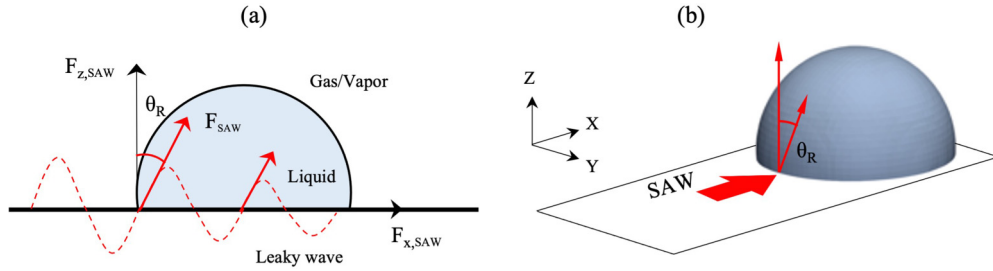


FIG. 1. (a) 2D illustration of SAW propagation along substrate. (b) 3D schematic of wave orientation and propagation.

Sheikholeslam Noori and co-workers [16,17] developed a two-dimensional (2D) droplet based SAW interaction model using the color-gradient LB methodology. The study reported the minimum amplitude required to initiate streaming, pumping, and jetting states for a lithium niobate (LiNbO_3) substrate at various resonant frequencies. Although promising, the findings are only for 2D cases hence further research is required in this field to develop 3D models able to fully capture the underlying mechanisms and simulate droplet dynamics as a consequence of SAW stimulated internal streaming.

The three-dimensional two-phase lattice Boltzmann model presented in this work is constructed and applied to simulate the kinetic impact from a SAW on a microscale sessile drop. SAW parameters (amplitude and frequency) are investigated and their influences on mixing, pumping, and jetting are analyzed. It is the objective of this study, and in addition the model development, to provide a comprehensive understanding of the roles that each parameter plays on SAW induced streaming and deformation.

II. SURFACE ACOUSTIC WAVE (SAW) DROPLET INTERACTION

Before moving to the model developed, a brief outline of the physics of SAW-droplet interactions is introduced which will aid in the discussion of the model setup and the results obtained. In general, it can be summarized that SAW propagates along the substrate in the direction of the liquid droplet. Upon entering the droplet, the acoustic wave is dampened exponentially, causing longitudinal pressure waves to be emitted through the liquid (see Fig. 1) at a Rayleigh angle, $\theta_R = \sin^{-1} \frac{C_f}{C_R}$, where C_f and C_R are the sound velocity in the liquid and the Rayleigh SAW velocity on the SAW substrate, respectively [5,18]. This initiates complex streaming patterns to emerge which can cause mixing, translation, or jetting of the droplet.

Due to the limitations of the experimental setup, these processes can be difficult to thoroughly study empirically, therefore it is necessary that computational methods are developed which can capture the two-phase flow pattern within the droplet, the deformation, and jetting. Due to the microscopic nature of these flow patterns, it only seems fitting that the chosen numerical model should be also. As a consequence, the LB methodology has been specifically chosen for this work. The lattice Boltzmann method (LBM) is a kind of mesoscopic model, lying between macroscopic and microscopic regimes, providing relatively high physical insight without the computational overhead of particle-based models, molecular

dynamics (MD) for example [19]. Additional benefits of the LBM are its ability to model complex boundary conditions, predict interfacial dynamics, and implement external forces with ease. This could be particularly beneficial in the exploration of SAW-based microfluidics involving curved or complex shaped devices.

In the following sections, the numerical model will be outlined and validated before SAW interactions are introduced. Numerical results will then be compared with experimental observations, validating the constructed model and culminating in a study of various LB parameters to determine their impact on droplet shape and motion.

III. CONSTRUCTION OF SAW-LATTICE BOLTZMANN MODEL

Based on the discussion in Sec. II, we consider that the liquid droplet is an incompressible fluid, for which the lattice Boltzmann model, derived from incompressible Navies-Stocks equations, can be applied. As such, a two-phase lattice Boltzmann-SAW interaction model is constructed for simulations of the dynamics of SAW impacts on the droplet. We consider the multiple-relaxation-time (MRT) scheme [20] in the pseudopotential LB framework to simulate multiphase fluid flows due to its suitability of implementing forces underpinned by underlying microscopic physics, in comparison with other multiphase models of LB frameworks, such as the color-gradient model [21,22], free-energy model [23,24], and phase-field model [25,26]. The details of each model can be found from the review papers [27,28].

A. Three-dimensional multiple-relaxation-time two-phase lattice Boltzmann model

In the LB community, the evolution equation with MRT collision operator can be written as [29]

$$f_i(\mathbf{x} + \mathbf{e}_i \delta_t, t + \delta_t) = f_i(\mathbf{x}, t) - \bar{S}_{ij}(f_j(\mathbf{x}, t) - f_j^{\text{eq}}(\mathbf{x}, t)) + \left(1 - \frac{\bar{S}_{ij}}{2}\right) F_i \delta_t \quad (1)$$

where f_i is the density distribution function, \mathbf{x} is the spatial position, \mathbf{e}_i is the discrete particle velocity along the i th direction, δ_t is the time step, f_j^{eq} is the equilibrium distribution function, F_i is the force term in discrete velocity space, and \bar{S}_{ij} is the collision matrix, expressed by [29]

$$\bar{S} = M^{-1} S M, \quad (2)$$

where \mathbf{M} is the orthogonal transformation matrix (given in Appendix A) and \mathbf{S} is the relaxation matrix, $\mathbf{S} = \text{diag}(s_\rho, s_e, s_\varepsilon, s_j, s_q, s_j, s_q, s_j, s_q, s_v, s_v, s_v, s_v, s_v, s_{xyz})$. For the D3Q15 lattice, the lattice velocities (\mathbf{e}_i) are given by

$$\begin{aligned} & [\mathbf{e}_0, \mathbf{e}_1, \mathbf{e}_2, \mathbf{e}_3, \mathbf{e}_4, \mathbf{e}_5, \mathbf{e}_6, \mathbf{e}_7, \mathbf{e}_8, \mathbf{e}_9, \mathbf{e}_{10}, \mathbf{e}_{11}, \mathbf{e}_{12}, \mathbf{e}_{13}, \mathbf{e}_{14}] \\ & = c \begin{bmatrix} 0 & 1 & -1 & 0 & 0 & 0 & 0 & 1 & -1 & 1 & -1 & 1 & -1 & 1 & -1 \\ 0 & 0 & 0 & 1 & -1 & 0 & 0 & 1 & 1 & -1 & -1 & 1 & 1 & -1 & -1 \\ 0 & 0 & 0 & 0 & 0 & 1 & -1 & 1 & 1 & 1 & 1 & -1 & -1 & -1 & -1 \end{bmatrix}, \end{aligned} \quad (3)$$

where $c = \delta_x/\delta_t = 1$ is the lattice constant.

The density distribution function f_i and equivalent equilibrium distribution f_i^{eq} can be found through projecting the distributions onto moment space via $\mathbf{m} = \mathbf{M}\mathbf{f}$, and $\mathbf{m}^{\text{eq}} = \mathbf{M}\mathbf{f}^{\text{eq}}$. Therefore, the right-hand side of Eq. (1) can be rewritten as

$$\mathbf{m}^* = \mathbf{m} - \mathbf{S}(\mathbf{m} - \mathbf{m}^{\text{eq}}) + \delta_t \left(\mathbf{I} - \frac{\mathbf{S}}{2} \right) \mathbf{M}\tilde{\mathbf{F}}, \quad (4)$$

where \mathbf{I} is the unit tensor, $\mathbf{M}\tilde{\mathbf{F}}$ is the forcing term in moment space with $(\mathbf{I} - \mathbf{S}/2)\mathbf{M}\tilde{\mathbf{F}} = \mathbf{M}\mathbf{F}'$, and the equilibrium moments \mathbf{m}^{eq} are given by

$$\begin{aligned} \mathbf{m}^{\text{eq}} = & \rho(1, -1 + |\mathbf{u}|^2, 1 - 5|\mathbf{u}|^2, u_x, -\frac{7}{3}u_x, u_y, -\frac{7}{3}u_y, u_z, \\ & -\frac{7}{3}u_z, 2u_x^2 - u_y^2 - u_z^2, u_y^2 - u_z^2, u_xu_y, u_yu_z, u_xu_z, 0)^T, \end{aligned} \quad (5)$$

where u_x , u_y , and u_z are the velocity components of the fluid in the x , y , and z directions, respectively. The magnitude of velocity is calculated through $|\mathbf{u}|^2 = u_x^2 + u_y^2 + u_z^2$. The streaming process of the MRT LB equation is implemented in velocity space as [30]

$$f_i(\mathbf{x} + \mathbf{e}_i\delta_t, t + \delta_t) = f_i^*(\mathbf{x}, t), \quad (6)$$

where $\mathbf{f}^* = \mathbf{M}^{-1}\mathbf{m}^*$. The macroscopic density ρ and velocity \mathbf{u} are acquired through

$$\rho = \sum_i f_i, \quad \rho\mathbf{u} = \sum_i \mathbf{e}_i f_i + \frac{\delta t}{2}\mathbf{F}, \quad (7)$$

where \mathbf{F} is the total force exerted on the system which includes, in this study, the interparticle force \mathbf{F}_{int} , adhesive force from solid boundaries, which can be treated through boundary conditions, and any external forces, e.g., the SAW force acting on the droplet, \mathbf{F}_{saw} , with $\mathbf{F} = \mathbf{F}_{\text{int}} + \mathbf{F}_{\text{saw}} = (F_x, F_y, F_z)$. The forces are introduced as follows.

1. Fluid-fluid interactions

In the pseudopotential model [31,32], multiphase flow phenomena are established via an interaction force which aims to mimic molecular interactions. For a single component, the interaction force is given by

$$\mathbf{F}_{\text{int}} = -G\psi(\mathbf{x}) \sum_{i=1}^N w(|\mathbf{e}_i|^2) \psi(\mathbf{x} + \mathbf{e}_i\delta_t) \mathbf{e}_i, \quad (8)$$

where G is the interaction strength, $\psi(\mathbf{x})$ is the interaction potential, and $w(|\mathbf{e}_i|^2)$ are the weights, given by $w(1) = 1/3$ and $w(2) = 1/24$ with $N = 14$ for nearest-neighbor interactions on a D3Q15 lattice. The thermodynamic pressure p , related to the pseudopotential in the pseudopotential model, is given

by $p = \rho c_s^2 + \frac{Gc^2}{2}\psi^2$ with the lattice sound speed $c_s = c/\sqrt{3}$. The definition and calculations of the pseudopotential are given and discussed in Sec. IV A.

In an attempt to introduce adjustable interfacial tension into MRT models, Li *et al.* [30] suggest the addition of a source term \mathbf{C} into the MRT LB equation,

$$\mathbf{m}^* = \mathbf{m} - \mathbf{S}(\mathbf{m} - \mathbf{m}^{\text{eq}}) + \delta_t \left(\mathbf{I} - \frac{\mathbf{S}}{2} \right) \mathbf{M}\tilde{\mathbf{F}} + \delta_t \mathbf{C}, \quad (9)$$

where the forcing term in moment space $\mathbf{M}\tilde{\mathbf{F}}$ is defined as [33]

$$\begin{aligned} \mathbf{M}\tilde{\mathbf{F}} = & \left(0, 2\mathbf{u} \cdot \mathbf{F} + \frac{6\sigma|\mathbf{F}|^2}{\psi^2\delta_t(s_e^{-1} - 0.5)}, -10\mathbf{u} \cdot \mathbf{F}, F_x, \right. \\ & -\frac{7}{3}F_x, F_y, -\frac{7}{3}F_y, F_z, -\frac{7}{3}F_z, 4u_xF_x - 2u_yF_y \\ & - 2u_zF_z, 2u_yF_y - 2u_zF_z, u_xF_y + u_yF_x, u_yF_z \\ & \left. + u_zF_y, u_xF_z + u_zF_x, 0 \right)^T, \end{aligned} \quad (10)$$

with the parameter σ used to alter the mechanical stability of the model [34], ensuring thermodynamic consistency. Additionally, the source term \mathbf{C} is defined to adjust the interfacial tension, with variables Q_{xx} , Q_{yy} , Q_{zz} , Q_{xy} , Q_{yz} , and Q_{xz} obtained from [33]

$$\begin{aligned} \mathbf{C} = & \left(0, \frac{4}{3}s_e(Q_{xx} + Q_{yy} + Q_{zz}), 0, 0, 0, 0, 0, 0, 0, \right. \\ & -s_v(2Q_{xx} - Q_{yy} - Q_{zz}), -s_v(Q_{yy} - Q_{zz}), \\ & \left. -s_vQ_{xy}, -s_vQ_{yz}, -s_vQ_{xz}, 0 \right)^T, \end{aligned} \quad (11)$$

$$\mathbf{Q} = \kappa \frac{G}{2} \psi(\mathbf{x}) \sum_{i=1}^N w(|\mathbf{e}_i|^2) [\psi(\mathbf{x} + \mathbf{e}_i) - \psi(\mathbf{x})] \mathbf{e}_i \mathbf{e}_i, \quad (12)$$

where κ is used to adjust the interfacial tension γ . According to [30], the addition of $(1-\kappa)$ in the discrete form pressure tensor is intended to allow the interfacial tension to decrease and approach zero as κ increases from 0 to 1. Note that the term \mathbf{C} is introduced for interfacial tension adjustment therefore it is constructed solely by fluid interactions predicted by Eq. (12) without other forces. The above methodology provides flexibility and stability in the model to simulate fluid flows at high density ratio and low viscosity, while allowing for adjustable interfacial tension.

2. Fluid-solid interactions

Incorporating adhesive effects between solids and fluids in the pseudopotential LB scheme has been widely studied. Generally, there have been two main methodologies developed to mimic fluid-solid interactions, namely the

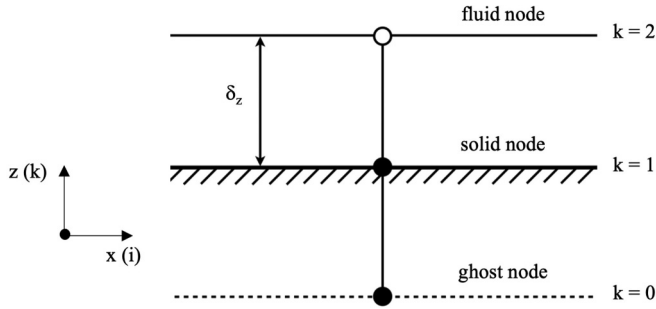


FIG. 2. 2D Schematic of geometric formulation wetting boundary condition.

density-based interaction [35,36] and the pseudopotential-based interaction [37–39]. For the density-based interaction models a fictitious wall density is introduced at the solid nodes, whereas for pseudopotential-based interactions schemes, a pseudopotential is adopted at the solid nodes. Li *et al.* [40] comprehensively studied these schemes and proposed an alternative approach. In their method, aptly named the modified-pseudopotential interaction model, they replace the constant pseudopotential at the solid nodes with that of the fluid-fluid interactions, resulting in a fluid-solid forcing of the same order of magnitude as $\psi(\mathbf{x} + \mathbf{e}_i \delta_i)$ in Eq. (8).

Recently, the geometric wetting condition [41], originating in the phase-field LB method, has been adopted to incorporate wetting phenomena in the multiphase pseudopotential LB method [42,43]. In three dimensions $(x, y, z) = (i, j, k)$, with $z(k)$ at a direction perpendicular to the solid surface and $x, y(i, j)$ at directions along the solid surface [refer to Fig. 2 for a 2D (x, z) case], the scheme takes the following form [44]:

$$\rho_{i,j,0} = \rho_{i,j,2} + \tan\left(\frac{\pi}{2} - \theta\right)\zeta, \quad (13)$$

where

$$\zeta = \sqrt{(\rho_{i+1,j,1} - \rho_{i-1,j,1})^2 + (\rho_{i,j+1,1} - \rho_{i,j-1,1})^2} \quad (14)$$

and θ is the prescribed contact angle for adjustments of the wetting condition. The scheme requires a layer of ghost nodes adjacent to the solid boundary in order to calculate the value of density as shown in Fig. 2, which provides a simplistic schematic layout of each node (fluid, solid, and ghost) in two dimensions. The fluid layers are located at $k = 2$ and the solid boundary at $k = 1$, with the ghost layer located at the bottom of the domain $k = 0$. Unlike the fluid-solid methods detailed previously, the only requirement for this scheme is the definition of desired contact angle, hence no additional forcing is implemented. Calculation of the density in the ghost, solid, and adjacent fluid nodes is added to the rest of the computational domain, resulting in an accurate wettability condition. This scheme will be applied in this study.

3. Fluid-SAW interactions

As discussed in Sec. II, the emitted pressure waves generated from the SAW devices induce a body force in the liquid medium, instigating a circulatory motion within the fluid. A Rayleigh wave consists of two translational components [Fig. 1(a)]: one is longitudinal which causes horizontal

displacement, and the other is transverse producing vertical translation of the SAW. The motion of the surface particles is elliptical in a Rayleigh wave. When a liquid medium is loaded on to the surface of the piezoelectric substrate the vertical component of the acoustic wave couples with the liquid layer adjacent to the surface. This coupling leads to the emission of longitudinal waves into the liquid, known as the leaky Rayleigh wave or leaky SAW (LSAW).

Following our previous studies [11], the magnitude of the SAW force on the propagation path of an emitted SAW [at a given y location, refer to Figs. 1(a) and 1(b)] can be predicted by [45]

$$\mathbf{F}_{\text{SAW}} = -\rho(1 + \alpha_1^2)^{3/2} A^2 \omega^2 k_i \exp(2(k_i x + \alpha_1 k_i z)), \quad (15)$$

where $\omega = 2\pi f$ is the angular frequency, α_1 is the attenuation constant, A is the amplitude of the SAW [45], and the leaky SAW wave number $k_L = k_r + jk_i$ is a complex number with the imaginary part representing the energy dissipation within the liquid [9]. The attenuation constant can be found from $\alpha = j\alpha_1$ with $\alpha^2 = 1 - (C_L/C_R)^2$. The force is distributed in the x and z directions, respectively by Rayleigh angle θ_R , as shown in Fig. 1(a).

The SAW force is implemented in the numerical scheme as an external force in the pseudopotential method through \mathbf{F} . In physics, as discussed in Sec. II, the surface acoustic wave enters the liquid droplet upon reaching the interface, where the difference in sound speeds between the liquid and substrate causes it to radiate momentum into liquid along the Rayleigh angle. To introduce these effects into the model, a set of conditions are imposed to allow the forcing to only be active in the liquid phase. This is achieved via the average density of the domain which allows the model to distinguish between liquid and gas or vapor. By doing so a sharp cutoff is achieved through the interface and into the droplet, preventing any SAW forcing from being active in the gas or vapor phase. Additionally, the contact points of the droplet are continuously monitored to ensure the droplet is still in contact with the SAW substrate. Once the droplet leaves the surface, the forcing (SAW) is inactive as is that in the physical experiments.

IV. LBM MODEL VALIDATION AND DISCUSSION

In the following we validate the model using conventional benchmark tests to demonstrate its capability and applicability to the current study.

A. Evaluation of thermodynamic consistency

In order to evaluate the thermodynamic consistency of the model, we compare the numerically obtained coexistence curves against the analytical Maxwell construction through simulating flat interfaces. Yuan and Schaefer [46] proposed a method of incorporating various equations of state (EOSs) into the single-component pseudopotential model through a square-root formulation,

$$\psi(\mathbf{x}) = \sqrt{2(p - \rho c_s^2)/Gc^2}, \quad (16)$$

where p is the thermodynamic pressure that can be calculated by fluid EOSs to present the fluid interactions. In this study

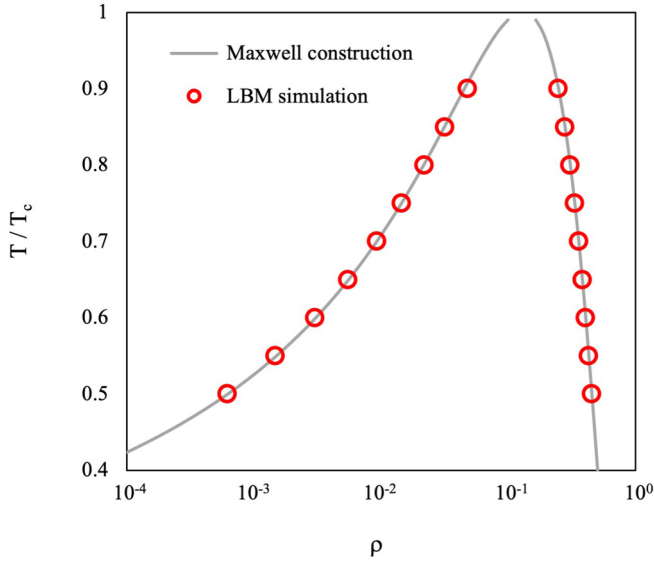


FIG. 3. Comparison of numerical coexistence curve with the analytical curve predicted by Maxwell construction.

the Carnahan-Starling (CS) EOS is adopted [46],

$$p = \rho RT \frac{1 + b\rho/4 + (b\rho/4)^2 - (b\rho/4)^3}{(1 - b\rho/4)^3} - a\rho^2, \quad (17)$$

where $a = 0.4963R^2T_c^2/P_c$ and $b = 0.18727RT_c/P_c$ with $T_c = 0.37733a/(bR)$. The parameters a , b , and R are set to $a = 0.25$, $b = 4$, and $R = 1$, respectively. Equation (17) is applied to predict the thermodynamic pressure for estimations of the component pseudopotential, $\psi(\mathbf{x})$, for fluid-fluid interactions, Eq. (8). It has been noted in the literature that the interface thickness can be adjusted by altering the value of a in the EOS [34]. When the square-root formulation is employed, the interaction strength G should be chosen such that the whole term inside the square root is always positive.

A domain size of $N_x \times N_y \times N_z = 100 \times 100 \times 100$ is implemented, with periodic boundary conditions applied in all directions. The density field is initialized as

$$\rho(x, y, z) = \rho_g + \frac{\rho_l - \rho_g}{2} [\tanh(z_1) - \tanh(z_2)], \quad (18)$$

where $z_1 = 2(z-25)/W$ and $z_2 = 2(z-75)/W$, with $W = 5$ as the initial interface thickness. Following Xu *et al.* [33], the value of σ in Eq. (10) is set to 0.12 in all simulations unless stated otherwise.

The coexistence curves shown in Fig. 3 are in agreement with the Maxwell construction, demonstrating the scheme's capability of capturing the saturate phase behavior of the fluid, even at large density ratios.

B. Evaluation of spurious currents

The introduction of spurious currents into the LB has been attributed to an imbalance in the discretization of forces in multiphase models [47]. This disparity can be amplified when simulating flows with large density differences, leading to numerical instability. Studies have been conducted in the LB community to mitigate their impact [48–50]; the details of

TABLE I. Maximum spurious velocities for SRT and MRT methods ($T_r = 0.5$)

		$\kappa = 0$	$\kappa = 0.5$	$\kappa = 0.95$
$s_v^{-1} = 0.6$	SRT	–	–	–
	MRT	0.055 411	0.056 327	0.067 002
$s_v^{-1} = 1.0$	SRT	0.040 350	0.034 532	0.027 726
	MRT	0.031 796	0.026 633	0.021 215

the discussion can be found from [47], a review of spurious currents in the LBM.

In this study, spurious velocities are evaluated to determine the performance of the current MRT model compared to the single-relaxation-time (SRT) model. Again following [33], the parameters in the relaxation matrix $\mathbf{S} = \text{diag}(s_\rho, s_e, s_\epsilon, s_j, s_q, s_j, s_q, s_j, s_q, s_\nu, s_\nu, s_\nu, s_\nu, s_\nu, s_{xyz})$ are selected as $s_\rho = s_j = 1.0$, $s_e = s_\epsilon = s_q = 1.1$, and $s_{xyz} = 1.2$ for the MRT model, while the relaxation rates in the SRT model are equal to each other, $s_\rho = s_j = s_e = s_\epsilon = s_q = s_{xyz} = s_\nu$. A lattice size of $N_x \times N_y \times N_z = 120 \times 120 \times 120$ is adopted in the simulations, with a spherical droplet of radius $R_d = 30$ initially positioned in the center of the domain. Periodic boundary conditions are applied in all three directions and the density field is initialized as follows:

$$\rho(x, y, z) = \frac{\rho_l + \rho_g}{2} - \frac{\rho_l - \rho_g}{2} \tanh \left[\frac{2(R_c - R_d)}{W} \right], \quad (19)$$

where $R_c = \sqrt{(x - x_0)^2 + (y - y_0)^2 + (z - z_0)^2}$, with (x_0, y_0, z_0) being the center of the computational domain, and $W = 5$ is the initial interface width. The reduced temperature is set to $T_r = 0.5$ which corresponds to a density ratio of $\rho_l/\rho_g \approx 750$.

It is found from the simulations that the maximum spurious velocities are all materialized outside of the droplet. From Table I it shows that MRT provides a reduction of spurious velocities, while also enhancing the numerical stability of simulations over SRT models. Interestingly at $s_v^{-1} = 1.0$ spurious velocities are reduced with an increase in parameter κ (decrease in interfacial tension), however when $s_v^{-1} = 0.6$ the opposite is witnessed.

Additionally, the maximum spurious velocities for the whole domain as well as those inside the droplet at $T_r = 0.5$ are plotted against s_v^{-1} , shown in Fig. 4. It is found that the maximum spurious velocity in the whole domain is smaller than 0.04 for $s_v^{-1} \geq 0.65$, however as $s_v^{-1} < 0.65$ this increases to around 0.06 then finally to approximately 0.14 for $s_v^{-1} = 0.53$. Conversely, the magnitude inside the droplet is small and remains fairly constant over the range of s_v^{-1} only increasing once $s_v^{-1} < 0.6$. The spurious velocities inside the droplet and the effects on simulation SAW-droplet interactions will be discussed in Sec. V A 1 for details.

C. Evaluation of Laplace's law

Laplace's law is employed to validate the simulation of droplets of different radii. According to Laplace's law, the pressure difference across the interface of a spherical drop is related to the interfacial tension and the radius of the drop. In three dimensions, the law is given by $\delta p = p_{\text{in}} - p_{\text{out}} =$

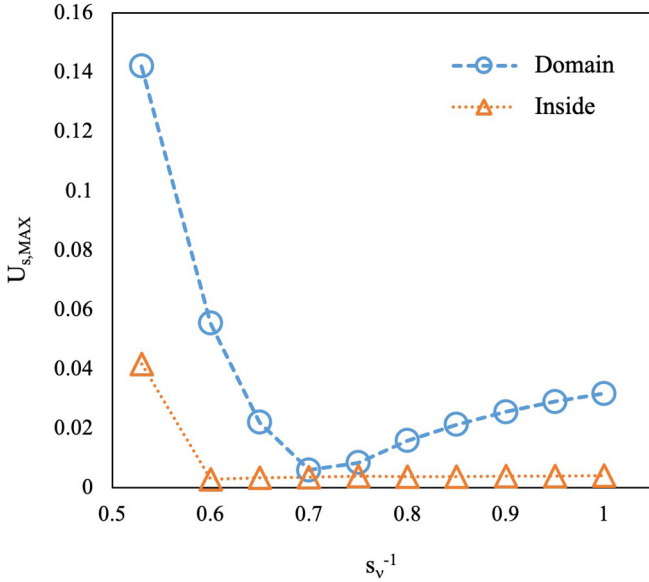


FIG. 4. Maximum spurious velocities for whole domain and inside droplet at $T_r = 0.5$.

$2\gamma/R_d$, where p_{in} and p_{out} are the fluid pressures inside and outside of the drop, respectively. Once the interfacial tension is given, the pressure difference will be proportional to $1/R_d$.

Simulations are carried out under the same cases set in Sec. IV B. To test the relationship numerically, the radius of the droplet is varied within $20 < R_d < 40$, and the pressure difference is obtained. Additionally, the adjustment of the interfacial tension via Eq. (12) is validated for $\kappa = 0$, $\kappa = 0.5$, and $\kappa = 0.95$. As shown in Fig. 5, a linear relationship is confirmed for all cases with the coefficients of determination being 0.9986, 0.9976, and 0.9860, respectively. The model demonstrates a proportional relationship between the pressure difference inside and outside of the drop, and the inverse of drop radius, thus Laplace's law is substantiated.

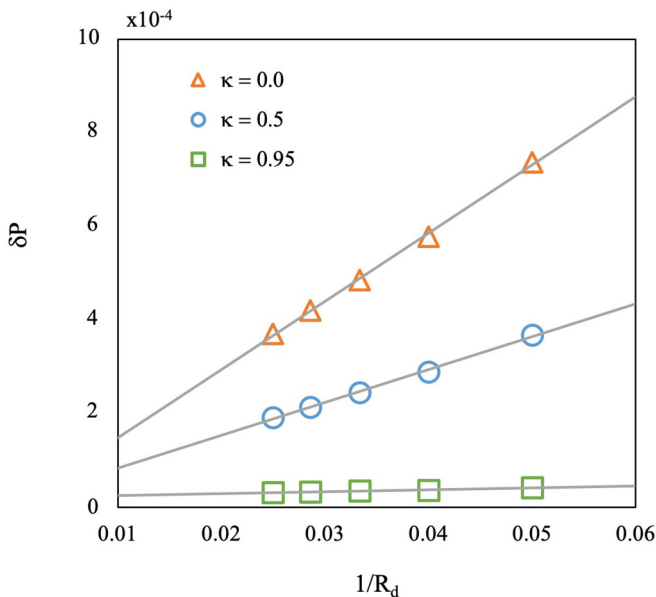


FIG. 5. Numerical validation of Laplace's law.

D. Evaluation of contact angle

A liquid droplet placed on a flat solid surface will exhibit an equilibrium state of either partial or complete wetting [51]. During partial wetting, the free energy of each phase (solid, liquid, and gas or vapor) is in equilibrium, with the interfacial tension balance at the three-phase contact line being represented by Young's equation,

$$\gamma_{SV} - \gamma_{SL} - \gamma_{LV} \cos \theta_y = 0, \quad (20)$$

where γ_{SV} , γ_{SL} , and γ_{LV} represent the interfacial tensions of solid-gas or vapor, solid-liquid, and liquid-gas or vapor interfaces, respectively, with the macroscopic contact angle being equal to the microscopic contact angle θ_y [52]. Considering the above, we evaluate the simulated static contact angle against the analytical solution using the geometric formulation. In the simulations, a stationary semispherical droplet of radius $R_d = 25$ is initially placed on a flat surface with no body force applied. A lattice size of $N_x \times N_y \times N_z = 120 \times 120 \times 80$ is adopted, with periodic boundary conditions applied in the x and y directions, while a no-slip condition is added to the upper and lower boundaries. As previously, the reduced temperature is set to $T_r = 0.5$. The results in Fig. 6 show good agreement with the analytical solution (Table II in Appendix B), demonstrating the capability of the model to simulate static contact angles accurately.

E. Evaluation of droplet oscillation

Since the nature of the study requires evaluation of droplet dynamics, a dynamic validation case is presented. Here we simulate an oscillating droplet, which is initially placed at the center of the domain and deformed to an ellipsoidal shape by

$$\frac{(x - x_0)^2}{R_d^2} + \frac{(y - y_0)^2}{R_d^2} + \frac{(z - z_0)^2}{(0.8R_d)^2} = 1, \quad (21)$$

where (x_0, y_0, z_0) is the center of the domain and initially set as $R_d = 30$. The frequency of the n th mode oscillation is given by Miller and Scriven [53],

$$\omega_n = \omega_n^* - \frac{1}{2}\alpha\omega_n^{*2} + \frac{1}{4}\alpha^2, \quad (22)$$

where ω_n is the angular response frequency and ω_n^* is Lamb's natural resonance frequency [54],

$$(\omega_n^*)^2 = \frac{n(n+1)(n-1)(n+2)}{R_e^3[n\rho_g + (n+1)\rho_l]}\gamma, \quad (23)$$

where R_e is the radius of the drop at equilibrium. The parameter α in Eq. (22) is given by [53]

$$\alpha = \frac{(2n+1)^2(\mu_l\mu_g\rho_l\rho_g)^{1/2}}{\sqrt{2}R_e[n\rho_g + (n+1)\rho_l][(\mu_l\rho_l)^{1/2} + (\mu_g\rho_g)^{1/2}]}, \quad (24)$$

where μ_l and μ_g are the dynamic viscosities of the liquid and gas or vapor phases, respectively, with $\mu = \rho\nu$. Due to the effect of interfacial tension and viscous dampening, the ellipsoidal droplet oscillates until a spherical shape is reached, with the amplitude of the oscillations decreasing over time. Figure 7 illustrates the evolution of the normalized droplet radius in both the horizontal and vertical directions. At the intersection of the solid and dashed lines, the droplet is spherical in shape.

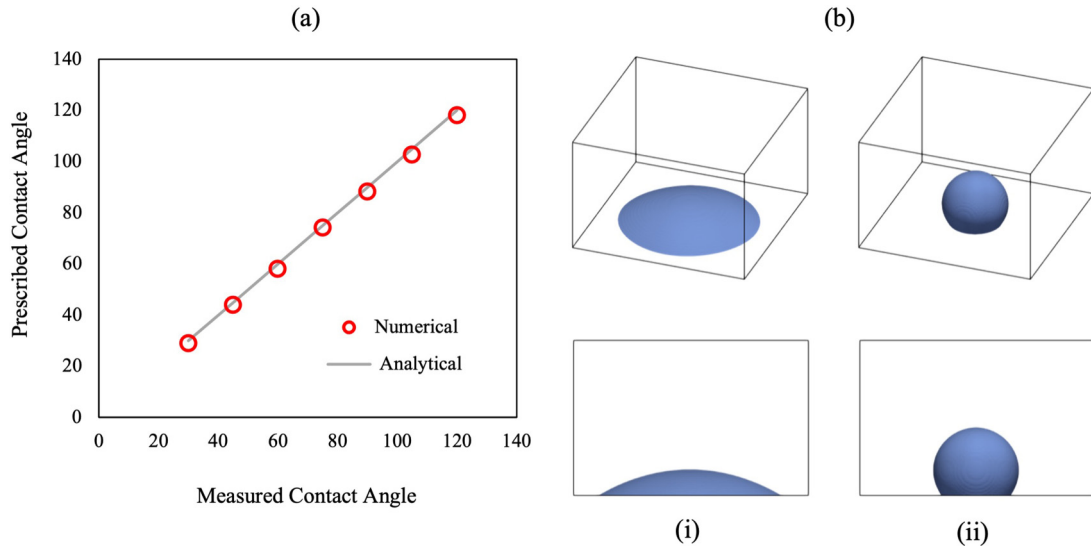


FIG. 6. Simulated contact angles using geometric formulation. (a) Validation against analytical solution. (b) (i) $\theta \approx 30^\circ$, (ii) $\theta \approx 120^\circ$.

The analytical solution of the time period $T' = 2\pi/\omega_n$ for the second mode ($n = 2$) obtained from Eq. (22) is compared to the simulation result. The analytical oscillatory period is found as $T' = 2601$, while the numerical oscillation period is $T_{LBM} = 2748$, giving a relative error of 5.7%. Additionally, we study the influence of interfacial tension on the droplet oscillations by varying the parameter κ , in Eq. (12), $0 < \kappa < 0.5$. The numerical and analytical oscillation periods for $\kappa = 0.25$ are $T' = 3016$ and $T_{LBM} = 3211$, respectively, while for $\kappa = 0.5$, $T' = 3748$ and $T_{LBM} = 3950$. The relative errors being 6.5% and 5.4% are consistent with those reported in the literature [55].

V. NUMERICAL ANALYSIS OF SAW INTERACTIONS ON A DROP

In the subsequent section, we apply the constructed SAW-LB model to study the effects of SAW interactions on a droplet to demonstrate how the constructed model can simulate and predict the internal physics and dynamics before

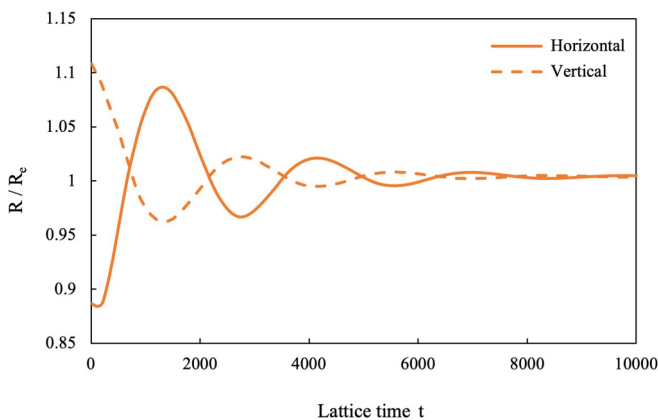


FIG. 7. Normalized radius of oscillatory droplet as a function of time for $\kappa = 0$.

further applications. Following the computational setup, the model is first validated then the effects of parameters such as wave amplitude, frequency, surface wettability, viscosity ratio, and interfacial tension on droplet are examined. Thermal and aperture effects are not considered in this study. The mesh independent and grid resolution tests identify a mesh of $N_x \times N_y \times N_z = 5R_d \times 3R_d \times 4R_d$, with a drop radius of $R_d = 40$, to capture the flow dynamics with optimized computational cost. In the simulations, a semispherical droplet of radius $R_d = 40$ initially placed on the bottom surface with initial contact angle $\sim 100^\circ$ and its center at (100, 60, 5), unless stated otherwise. The setup of the simulation can be referred to in Fig. 8, including the boundary conditions. The reduced temperature is again set to $T_r = 0.5$, equivalent to a density ratio of $\rho_l/\rho_g \approx 750$ ($\rho_l = 0.454$, $\rho_g = 0.0006$) with $\nu_g/\nu_l \approx 15$. The parameter σ in Eq. (10) is set to 0.12 in order to achieve thermodynamic consistency and $s_v^{-1} = 0.5077$ is set for the liquid phase to provide appropriate conversion parameters to match the interfacial tension between physical and LB. Periodic boundary conditions are applied in the x and y directions, while a no-slip condition is added to the upper and lower boundaries. The droplet is first allowed to reach an

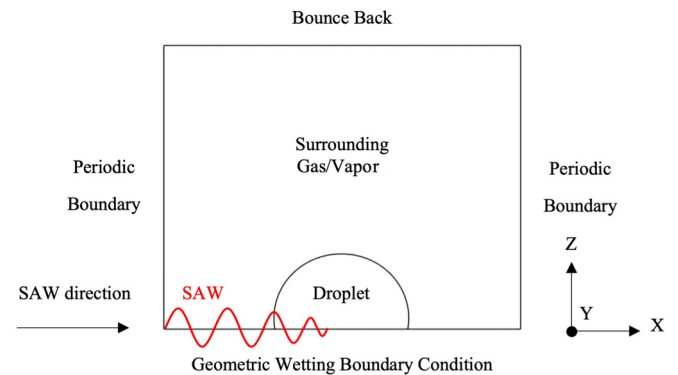


FIG. 8. Schematic of the setup of simulations and the boundary conditions.

equilibrium state on the SAW substrate, after which the SAW interactions are introduced.

A. Model validation

To validate the SAW interactions in the LB model, the simulation results are quantitatively compared with experimental data, which are taken from the selected records of previous experiments described in Ref. [56]. Three different modes are considered; *mixing*, *pumping*, and *jetting*, which will demonstrate the applicability of the proposed methodology to SAW based microfluidics applications. A set of nondimensional groups have been chosen to allow for comparison between numerical and experimental data, which are Reynolds number, Weber number, and capillary number, defined as $Re = \frac{\rho_l u D}{\mu_l} = \frac{u D}{\nu_l}$, $We = \frac{\rho_l u^2 D}{\gamma}$, and $Ca = \frac{\mu_l u}{\gamma}$ with D the droplet diameter, u the droplet velocity, and γ the interfacial tension. Note that the velocity definition for pumping is the mean velocity, summarized as the movement of the droplet along the surface, whereas for jetting it is along the length of the droplet from initial state until the drop is ejected from the surface.

Physical parameters are related to lattice units through unit conversion. To properly convert between the LB and physical domains, three independent primary conversion factors are required. In this work, a droplet of water with volume $5 \mu\text{l}$ and initial radius of 1.34 mm is studied, which corresponds to a length scale conversion $C_l = 33.4 \mu\text{m}$. Physical properties of water at 20°C are taken as [57] $\rho_w = 998.2 \text{ kg m}^{-3}$, $\nu_w = 1.004 \times 10^{-6} \text{ m}^2 \text{ s}^{-1}$, and $\gamma_w = 0.07273 \text{ N m}^{-1}$. The consequent time conversion factor is $C_t = 2.85 \times 10^{-6} \text{ s}$, with a velocity scale conversion calculated as $C_u = C_l/C_t = 11.72 \text{ m s}^{-1}$. LiNbO₃ based SAW devices were used, with designed wavelengths of 64, 32, 20, and 12 microns, corresponding to the measured frequencies of 61.7, 110.8, 199.4, and 250.1 MHz, which were reported in detail in a previous publication [56]. SAW parameters applied in the simulations are representative of LiNbO₃ substrate, where $\alpha_1 = 2.47$ and $k_i = -1370 \text{ m}^{-1}$ [45] in Eq. (15).

1. SAW streaming

We primarily analyze the first mode, mixing or streaming, against experimental data. At low magnitude of SAW power, the droplet is able to stay in its original place and undergoes minimal deformation. This is due to the interfacial tension effect being high enough to withstand the SAW interaction. From experiments [56] they investigated the effect of increasing frequency to determine the threshold power to achieve streaming inside the droplet, revealing that an increase in SAW power is required, i.e., 0.2 W at 61.7 MHz to 0.47 W at 250.1 MHz.

Consequently, in the LB simulations a similar outcome is achieved. As shown in Fig. 9, the droplet is slightly elongated in the z direction however it remains pinned to the surface even after a few milliseconds. For the range of resonant frequencies, a minimum amplitude is required to initiate mixing inside the droplet. Below this threshold amplitude SAW based streaming does not occur. Instead unphysical spurious currents dominate, showcasing symmetrical flow patterns inside the drop which can be mistaken

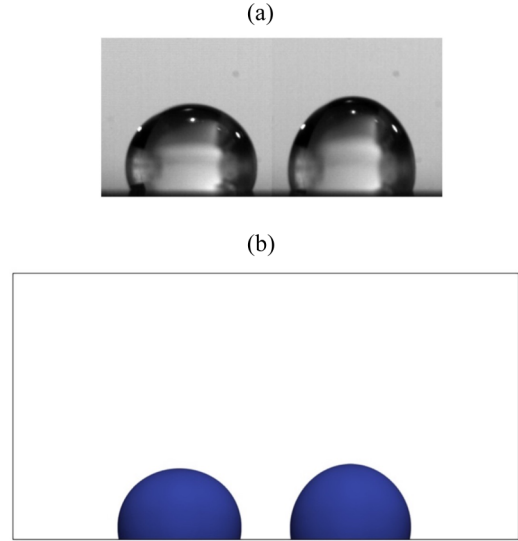


FIG. 9. (a) Experimental images of deformation phenomena due to streaming for $5\text{-}\mu\text{l}$ droplet operated at 61.7 MHz and low power of 0.2 W and (b) LB simulation results.

for streaming, ranging in order of magnitude from 10^{-2} to 10^{-5} (in lattice units) depending on the area of droplet being examined. In this study, we have studied four different resonant frequencies as introduced previously. It is demonstrated that only a small change in SAW amplitude is required between frequencies to achieve mixing phenomena inside the drop.

A major concern of implementing the pseudopotential model in the study of SAW streaming and its effect on droplet dynamics is the presence of spurious (parasitic) velocities. In the following we investigate these effects and aim to clarify at which range of wave amplitude are spurious velocities no longer dominant and streaming can be predicted. We focus on a resonant frequency of 61.7 MHz and alter the interfacial tension through 0.055–0.092 N/m. A range of wave amplitudes are studied and compared to a droplet at rest, on a SAW substrate surface, without any SAW interaction. The flow field and velocity profiles, across the width of the drop, are analyzed. The culmination of the data reveals a threshold amplitude at which streaming or mixing can be achieved for each value of interfacial tension (Fig. 10). The areas above and below this threshold have been termed as *streaming dominant* and *spurious dominant*, respectively, to reflect the flow field attained. In our analysis we have defined streaming dominant as an internal flow structure and velocity profile which resembles the research in Ref. [11] while spurious dominant is outlined as a symmetrical velocity field, comparable to that of a droplet on a solid surface without any SAW interactions.

As shown in Fig. 11, the magnitude of wave amplitude plays an important role in the formation of streaming inside the droplet. Comparing low amplitude and hence low power [Figs. 11(c) and 11(d)] to the droplet without SAW interaction [Figs. 11(a) and 11(b)], we see similarities. First, the flow field and velocity vectors are comparable with central vortices dominating. Also, taking a profile across the droplet we see the largest velocity magnitude at the edges, close to the in-

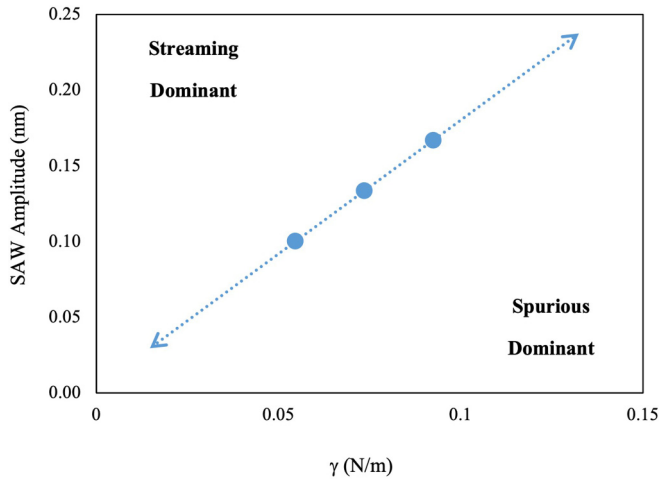


FIG. 10. SAW amplitude for different interfacial tensions at which streaming or mixing is induced for 61.7 MHz. Above dotted line is streaming dominant and below is spurious current dominant.

interface, yielding a parabola distribution. The main differences between the two sets of data are that the velocity has been increased with SAW forcing and the flow field no longer has exact symmetry. This type [Figs. 11(c) and 11(d)] can be categorized as a spurious dominant flow. As the amplitude is further increased, we see a velocity distribution depart from symmetry to that which resembles a mixing scenario. Looking at Figs. 11(e) and 11(f), we see large velocities on the left-hand side of the droplet, above the interaction area, and a vortex located at the right side. Additionally, the velocity profile reflects this with a large magnitude close to the interaction point, diminishing along the length with smaller peaks near the center and far side of the droplet. The velocity distribution in Fig. 11(f) is the same as those found in Fig. 10(a) of [11] by experiments and computational fluid dynamics (CFD) modeling, hence we classify it as a streaming dominant flow.

We conduct similar tests for two further interfacial tension variations. Comprehensive results can be found in Appendix C. From this study it has been discovered that an increase in interfacial tension requires an increase in wave amplitude to elicit a streaming mode within the droplet. This can be partly attributed to the increased spurious velocities inside the droplet which are a consequence of the interfacial tension at the intermolecular level. The increased interaction force between phases causes a higher magnitude of currents to be established at the interface. To overcome these currents, a stronger SAW force is required to manipulate and rearrange into a streaming pattern, as shown in Fig. 10.

In this study, results obtained for mixing or streaming are all from simulations in the streaming dominant regime, which are in good agreement with those from experiments, as shown in Fig. 9.

2. SAW pumping and jetting

Moreover, a further increase in SAW power provides additional momentum to the fluid along the Rayleigh angle. Increased circulatory motion within the droplet causes a wob-

bling effect in the initial few milliseconds, where the droplet is held in place although the interface moves upwards from left to right (Fig. 12). After this period, the droplet moves downwards which causes the rear contact area to begin to creep forward, hence a pumping state is initiated. As reported in Ref. [56], a larger disparity between SAW power is required to initiate pumping at lower frequency to high frequency than in the previous streaming mode.

In our research we have found that the nondimensional SAW amplitude (A/λ) is increased linearly with an increase in SAW frequency, until at high frequencies where the trend is downward (Fig. 14). Overall, the simulation data are approximately half those from the experiments for the range of frequencies. Unlike the mixing or steaming mode, during the pumping the droplet moves along the substrate. The interfacial tension between the fluid and the SAW substrate is not enough to withstand the body force applied during the SAW interaction. Comparing the shape obtained from the experiment to that in the simulation we see some differences. In the experiment the droplet is slightly more elongated to the right, with a tip being formed at the top. However, in the simulation we see no such feature. This could be a consequence of interfacial tension being dissimilar. Overall, the simulations are in agreement as there is some upward movement and slight asymmetry however not as pronounced as in the physical experiment. Additionally, when we look at the velocity comparison to the experimental data (Fig. 15) we find that the predictions are in good agreement. In each of the simulated cases, the model slightly overpredicts the velocity at the onset of the pumping mode. In our research, a pumping mode is initiated at $60 < Re < 140$, $0.02 < We < 0.1$, and $3 \times 10^{-4} < Ca < 7 \times 10^{-4}$, hence interfacial tension effects are dominant in this region.

When the SAW power is increased to such a point where the droplet is ejected from the surface, it is termed a jetting mode. Depending on the type of substrate being used, LiNbO_3 or zinc oxide film coated on silicon (ZnO/Si), the shape and overall motion of the jet can be different. The shape can vary from a thin beam [56] to full ejection of the droplet from the surface (Fig. 13). For ZnO/Si SAW devices [56], although able to achieve jetting effects, they require significantly more power for similar frequency than those for LiNbO_3 . This is an area which is planned for future research. For LiNbO_3 devices the droplet is ejected from the surface as the SAW energy transferred into the liquid is large enough to overcome those from interfacial tension and gravitational forces. A comparison between experimental and simulation results is presented in Fig. 13. The results are in good agreement with the shape and general motion of the LB simulations being comparable to those of the experiments.

From our research we have found that the ratio of SAW amplitude to SAW wavelength is almost linear with an increase in SAW frequency (Fig. 14). Up to frequencies of around 110.8 MHz, the simulation results are in close agreement with the experimental data. Above this frequency, the association starts to diminish. In the initial period the droplet is pushed upwards, elongating vertically and shrinking horizontally while the interface is deformed. As the SAW forcing is large, the left contact area is moved in the x direction toward the right contact area, causing a balloon shape to emerge. Once the con-

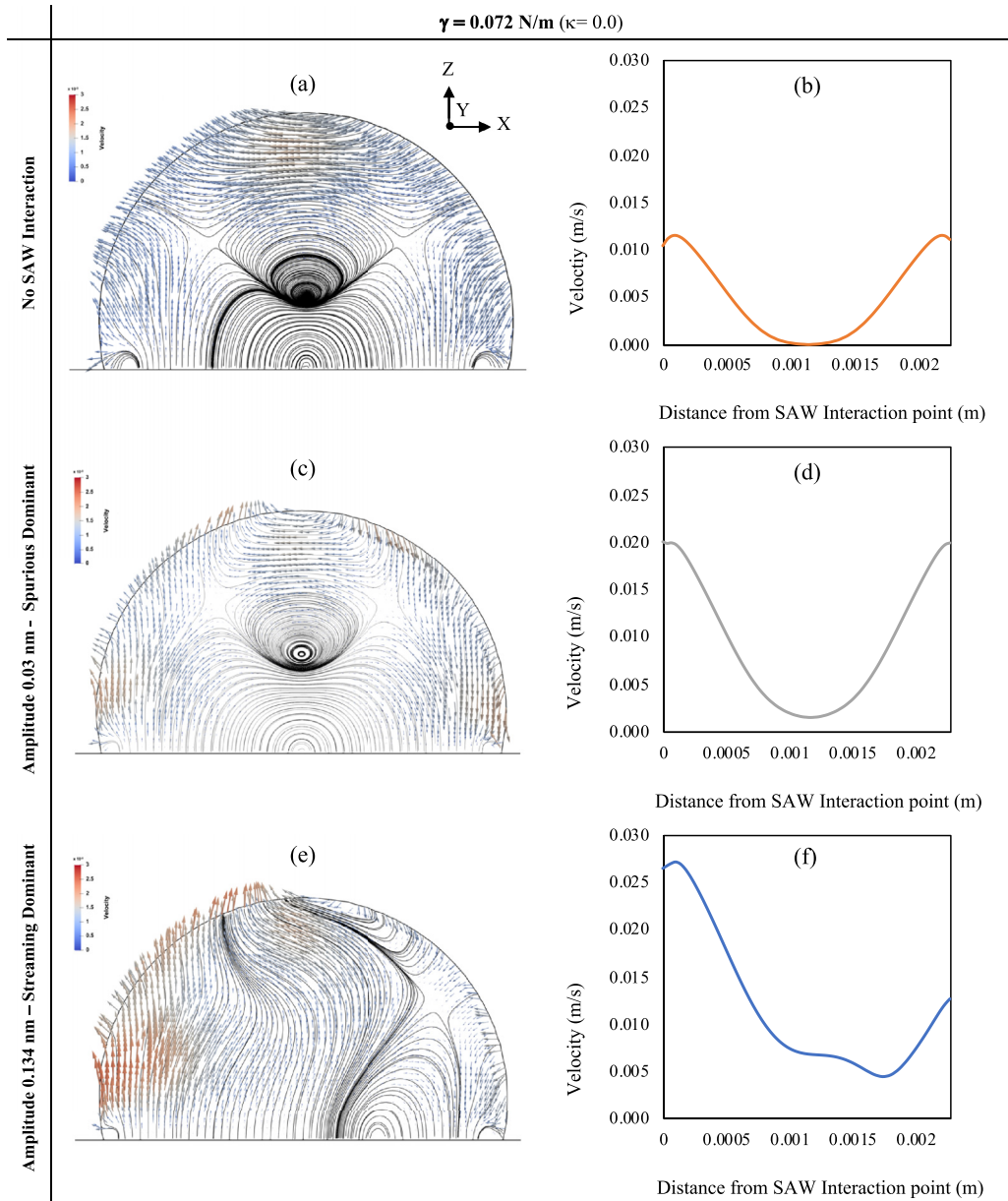


FIG. 11. Flow field and velocity profiles inside droplet at $\kappa = 0$ and 61.7 MHz. Droplet without SAW interaction (a),(b), and with SAW interaction; 0.03-nm wave amplitude (c),(d) and 0.134-nm wave amplitude (e),(f) (note: flow field in lattice units). View is slice through center of droplet at 17 ms.

tact area is small enough that the SAW forcing can overcome the interfacial tension, the droplet leaves the surface along the Rayleigh angle.

As shown in Fig. 15, the velocity data of the simulations alongside the experiment agree well. For a SAW device with frequencies of 61.7, 110.8, and 199.4 MHz the numerical velocity is overpredicted slightly, however with 250.1 MHz it is underpredicted quite considerably. In our analysis, the jetting mode commences at $230 < Re < 340$, $0.28 < We < 0.6$, and $1.2 \times 10^{-3} < Ca < 1.8 \times 10^{-3}$. In the study by Tan *et al.* [8] they witness the onset of single and multiple droplet ejection at Weber numbers of 0.1 and 0.4, respectively. We observe similar behavior since at $We < 0.1$ the droplet remains on the surface and undergoes a pumping action, as described previously (see Fig. 16).

In summary, the above comparison between experimental and LB simulation results demonstrates the ability of the proposed methodology for capturing the intricate dynamics of SAW interactions on a microscale sessile droplet. The validation of mixing, pumping, and jetting has been presented and analyzed. It is observed that there is a threshold wave amplitude at each frequency, at which the aforementioned modes can be achieved. Analysis of the data reveals that the amplitude present in the model is not consistent with the experimental trend. In spite of this, the results from the study are in good agreement with experimental findings, being within 4% relative error in velocity for pumping and jetting. In the following section, we will examine the effects of surface wettability on droplet dynamics when surface acoustic wave interactions are introduced.

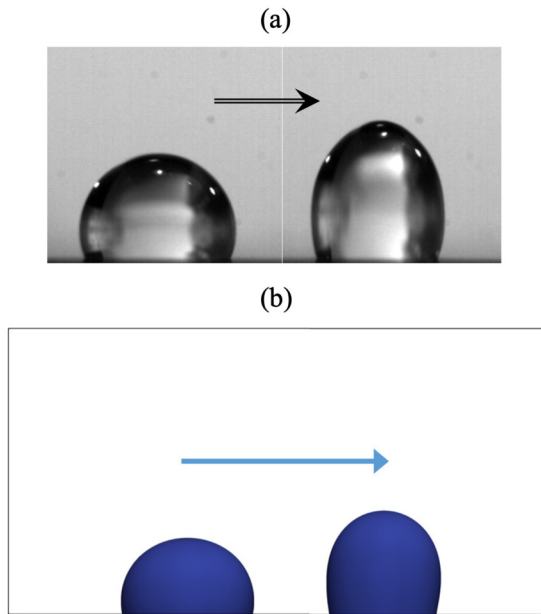


FIG. 12. (a) Experimental images of pumping phenomena for 5- μ l droplet agitated by SAW device with a frequency of 110.8 MHz and applied power of 1.2 W, (b) LB simulation results. Arrows show movement of droplet.

B. Effect of surface wettability

In this section, we analytically investigate the effect of surface wettability on droplet dynamics for the specific case of resonant frequency 199.4 MHz. All SAW parameters are kept constant with only the surface wettability being modified. We choose three wettabilities to be investigated; with initial static contact angles (θ_s) of 60°, 90°, and 120°. The shape and subsequent modes are analyzed to determine the effect the droplet contact angle has on SAW energy transfer into the droplet.

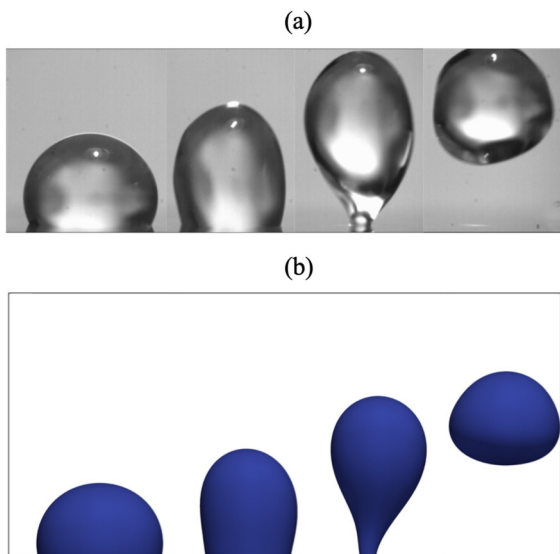


FIG. 13. (a) Experimental images of jetting mode for 5- μ l droplet agitated by SAW device with a frequency of 199.4 MHz and applied power 4.2 W, (b) LB simulation results.

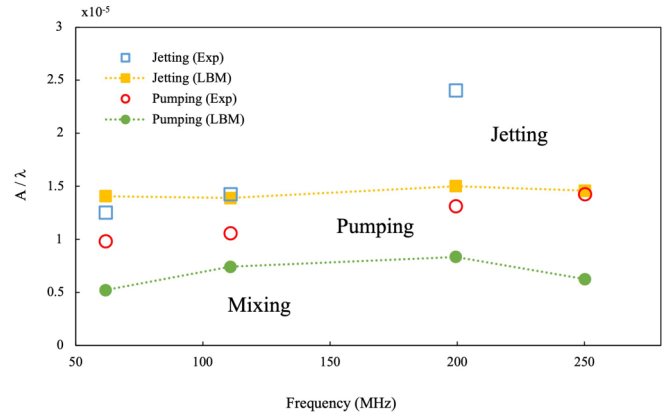


FIG. 14. Relationship between A/λ and frequency for transitioning between mixing, pumping, and jetting. (Experimental data extracted from [56].)

As shown in Fig. 17, a change in surface wettability can vastly alter the amount of SAW energy transferred into the droplet, resulting in different dynamics. For the hydrophilic surface (e.g., θ_s of 60°) the SAW interaction results in spreading with slight droplet movement. The increased interfacial tension, due to lower contact angle, is strong enough to overcome the SAW force. Moving to the surface with a static contact angle of 90°, we see no spreading on the SAW surface, while only a pumping state is achieved as the acoustic forcing is not sufficient to cause ejection from the surface. Again, this can be explained by an increased contact area being able to withstand the forcing for longer as compared to the hydrophobic surface. An increase in SAW power would be required to cause a transition from pumping to jetting at this wettability condition, as shown in Fig. 17.

The findings from the study reveal the importance of surface wettability to effectiveness of SAW energy transfer into the drop. At the same wave amplitude and frequency, through altering the wettability of the substrate, different modes can be achieved, intentionally or unintentionally. Careful design of the SAW device can allow for more efficient energy transfer, resulting in less power requirements. This can be particularly

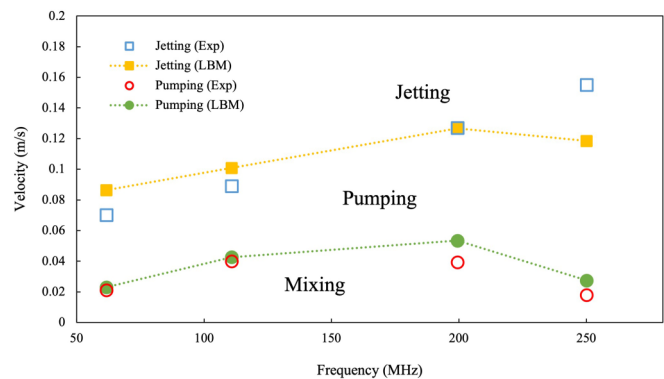


FIG. 15. Velocity of droplet as a function of resonant frequency at the transition from mixing to pumping (pumping data points) and pumping to jetting (jetting data points). (Experimental data extracted from [56].)

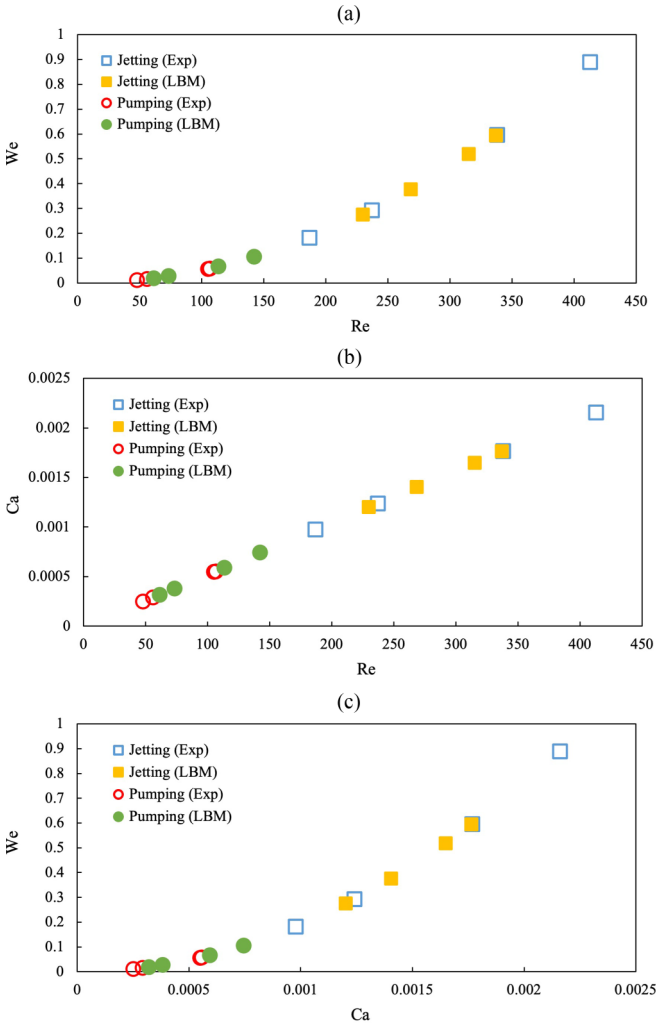


FIG. 16. Comparison between experimental [56] and simulated data (a) Weber number vs Reynolds number, (b) Capillary number vs Reynolds number, and (c) Weber number vs Capillary number.

useful for applications involving DNA where cells are susceptible to damage [58].

C. Effect of viscosity ratio

In this section we will investigate the effect of viscosity difference on droplet dynamics in the presence of surface acoustic wave interactions. Similar to previous, all computational parameters are kept constant with the exception of kinematic viscosity. In order to introduce a viscosity difference between the liquid and gas or vapor phase we adopt the conventional methodology, where $\nu(\rho) = \nu_l$ for $\rho > \rho_c$ and $\nu(\rho) = \nu_g$ for $\rho \leq \rho_c$ [34].

Considering the above treatments, three different cases are investigated for the present test: $\nu_g/\nu_l = 5$, $\nu_g/\nu_l = 15$, and $\nu_g/\nu_l = 20$. As before, a resonant frequency of 199.4 MHz has been assumed, with droplet shape and motion being compared when a jetting mode is witnessed.

As can be seen in Fig. 18(a), the effect of viscosity ratio on droplet dynamics is apparent. An increase in viscosity ratio has been shown to linearly increase the time taken for

the droplet to be ejected from the surface of the substrate. This delay in jetting can be explained due to the increased viscosity of the gas or vapor phase slowing the energy transfer as the droplet interface is moved along the Rayleigh angle. Another interesting aspect to note is the reduction in spurious velocities as a consequence of viscosity ratio [Fig. 18(b)]. The unphysical parasitic velocities which plague most multiphase LB models are those which can cause major instabilities in models, especially dynamic simulations. A reduction can be useful in both helping to stabilize the computational domain and when analyzing results.

D. Effect of interfacial tension

To analyze the effect of interfacial tension between the liquid and gas or vapor, we employ the Xu *et al.* method [33], described in Eq. (12), an extension of the already widely used methodology proposed by Li-Luo [30], to 3D space. It has been commented in the literature [59] that this approach is more effective for reducing interfacial tension whereas the scheme by Huang-Wu [60] is more suited to increasing interfacial tension. To the best of our knowledge, currently this strategy for interfacial tension adjustment has not yet been extended to 3D which is why the aforementioned has been selected for this work.

To study the effect of interfacial tension on droplet behavior, we look again at a resonant frequency of 199.4 MHz and a jetting regime. As before, we maintain the same computational setup with only the interfacial tension adjustment parameter κ being altered. We investigate a range of κ from -0.25 to 0.25 which will provide some insight into how increasing or decreasing interfacial tension affects the transfer of surface acoustic wave energy into the microdroplet.

The results illustrate the effect of modifying the interfacial tension between the droplet and the surrounding gas or vapor. At the moment just before the droplet is ejected from the surface, the shape and dynamics are scrutinized. Looking at Fig. 19, going from left to right, we see some differences in the droplet dynamics. At an increased interfacial tension ($\kappa = -0.25$) the droplet is slightly more balloon shaped and has more of a curvature, leaning further to the right, whereas with a reduced interfacial tension ($\kappa = 0.25$), the droplet is elongated further along the Rayleigh angle, with less curvature and balloon shape. This demonstrates that the interfacial tension has a strong influence on droplet shape however has less impact on droplet dynamics since, in all scenarios, the droplet is ejected from the substrate at approximately the same amount of time. Interestingly, the maximum velocity inside the droplet at the moment before ejection is altered as a result of interfacial tension adjustment. An increase in interfacial tension results in a rise in velocity of approximately 4.5% compared to the unmodified droplet. Similarly, when the interfacial tension is reduced, we see a lesser increase in maximum internal velocity of $\approx 1.6\%$.

VI. CONCLUSIONS

In summary, a three-dimensional numerical model for acoustic interactions with microscale sessile droplets under SAW excitation is developed, using a two-phase multiple

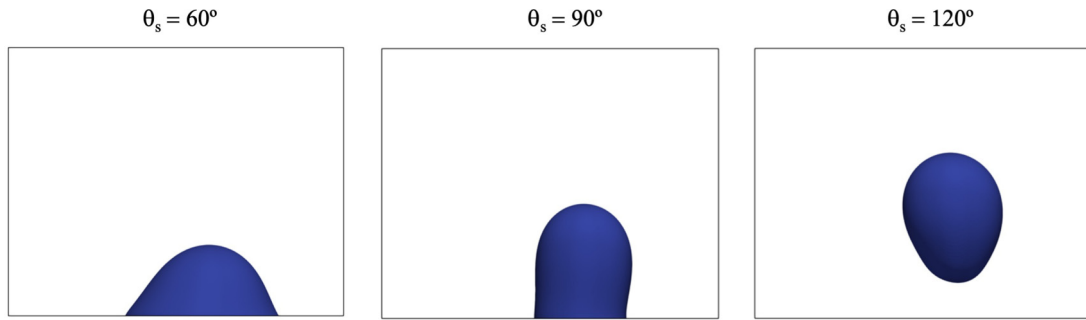


FIG. 17. Simulation results at 10 ms for resonant frequency 199.4 MHz at different surface wettabilities.

relaxation-time pseudopotential lattice Boltzmann method. The proposed model is initially validated against numerical benchmark tests. The results are in excellent agreement with the analytical solutions.

The developed model is then used in the study of SAW interactions with a microscale sessile droplet on a LiNbO₃ substrate. Simulation results are validated against experimental data, evaluating mixing, and pumping and jetting modes. A good agreement between simulations and experiments is achieved. The results demonstrate the applicability of the proposed methodology in the prediction of droplet dynamics subjected to SAW agitations. It is observed that there is a threshold wave amplitude at each frequency, at which the aforementioned modes can be achieved. Analysis of the data reveals that the amplitude in the model is not consistent with the experimental trend. Despite this, the results from the study are in agreement with experimental findings, being within 4% relative error in velocity for pumping and jetting. We observe the transition of mixing to pumping state at $We > 0.02$, $Ca > 3 \times 10^{-4}$, and $Re > 60$, with the onset of jetting mode at $We > 0.1$, $Ca > 1.2 \times 10^{-3}$, and $Re > 230$.

Furthermore, the effect of surface wettability on droplet dynamics is investigated. It is found that on hydrophilic surfaces, the energy transfer from the SAW to the droplet is impeded by the large interfacial tension force. This is in opposition to hydrophobic surfaces where the droplet is moved and ejected

from the substrate more easily. These results can be useful in the development of more efficient SAW devices.

Moreover, the effect of viscosity ratio and interfacial tension has been investigated when the droplet is subjected to SAW interactions. The findings reveal that viscosity ratio can play a role in delaying the ejection of the droplet from the surface. Movement of the liquid–gas or vapor interface is slowed resulting in a longer jetting time. Modification of the interfacial tension can lead to different droplet dynamics being witnessed. At larger interfacial tension, the droplet resists the deformation from the acoustic wave propagation, maintaining its spherical balloon shape. Alternatively, a reduction in interfacial tension allows the droplet to deform more along the Rayleigh angle, resulting in a longer jet to be seen. Focusing on the maximum internal jetting velocity, it is interesting to note that modifying the interfacial tension alters the velocity magnitude, nevertheless this has the inconsequential impact of the ejection time from the SAW substrate surface.

Having constructed a three-dimensional two-phase lattice Boltzmann model for simulating surface acoustic wave interactions on a droplet, it would be motivating to extend the method to include multiple components and thermal impacts. This has the potential to capture more realistic physics which could be used to broaden our understanding of the underlying mechanisms dictating the interaction between the acoustic wave and the fluid medium.

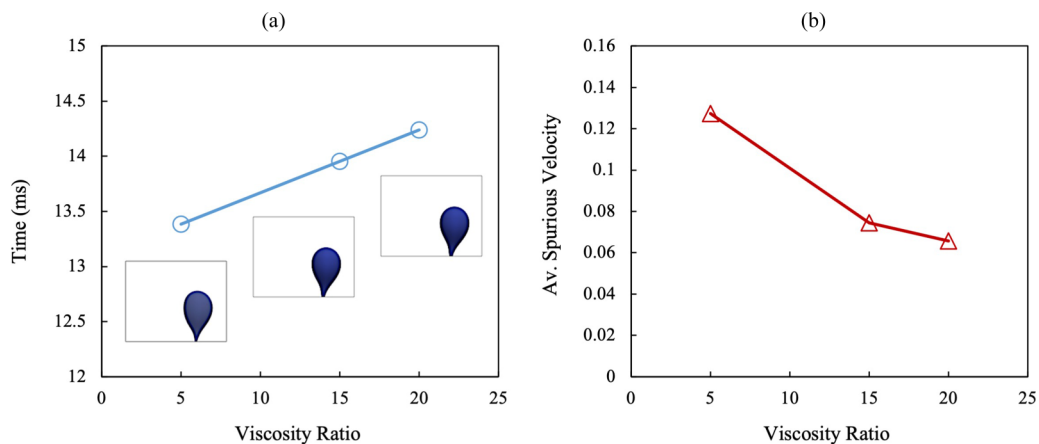


FIG. 18. Numerical results for jetting at resonant frequency 199.4 MHz. (a) Time for droplet to be ejected from surface against viscosity ratio. (b) Average spurious velocities, in the simulation domain, before SAW interaction against viscosity ratio.

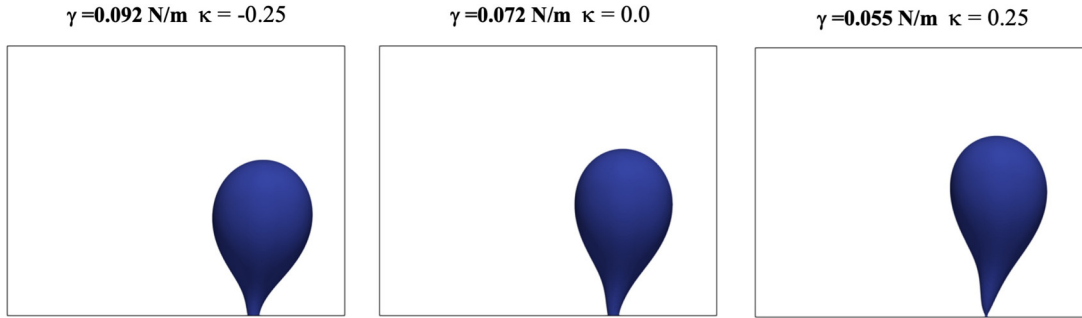


FIG. 19. Simulation results at 14 ms for resonant frequency 199.4 MHz at different interfacial tensions.

ACKNOWLEDGMENTS

S.B.B. was supported by EPSRC Doctoral Training Partnerships. The authors also acknowledge the financial support

from EPSRC Grant No. EP/P018998/1 and Special Interests Group of Acoustofluidics under the EPSRC-funded UK Fluidic Network (Grant No. EP/N032861/1).

APPENDIX A: ORTHOGONAL MATRIX FOR D3Q15 LATTICE

The transformation matrix for the D3Q15 LB model is given by [20].

$$M = \begin{pmatrix} 1 & 1 & 1 & 1 & 1 & 1 & 1 & 1 & 1 & 1 & 1 & 1 & 1 & 1 & 1 \\ -2 & -1 & -1 & -1 & -1 & -1 & -1 & 1 & 1 & 1 & 1 & 1 & 1 & 1 & 1 \\ 16 & -4 & -4 & -4 & -4 & -4 & -4 & 1 & 1 & 1 & 1 & 1 & 1 & 1 & 1 \\ 0 & 1 & -1 & 0 & 0 & 0 & 0 & 1 & -1 & 1 & -1 & 1 & -1 & 1 & -1 \\ 0 & -4 & 4 & 0 & 0 & 0 & 0 & 1 & -1 & 1 & -1 & 1 & -1 & 1 & -1 \\ 0 & 0 & 0 & 1 & -1 & 0 & 0 & 1 & 1 & -1 & -1 & 1 & 1 & -1 & -1 \\ 0 & 0 & 0 & -4 & 4 & 0 & 0 & 1 & 1 & -1 & -1 & 1 & 1 & -1 & -1 \\ 0 & 0 & 0 & 0 & 0 & 1 & -1 & 1 & 1 & 1 & 1 & -1 & -1 & -1 & -1 \\ 0 & 0 & 0 & 0 & 0 & -4 & 4 & 1 & 1 & 1 & 1 & -1 & -1 & -1 & -1 \\ 0 & 2 & 2 & -1 & -1 & -1 & -1 & 0 & 0 & 0 & 0 & 0 & 0 & 0 & 0 \\ 0 & 0 & 0 & 1 & 1 & -1 & -1 & 0 & 0 & 0 & 0 & 0 & 0 & 0 & 0 \\ 0 & 0 & 0 & 0 & 0 & 0 & 0 & 1 & -1 & -1 & 1 & 1 & -1 & -1 & 1 \\ 0 & 0 & 0 & 0 & 0 & 0 & 0 & 1 & 1 & -1 & -1 & -1 & -1 & 1 & 1 \\ 0 & 0 & 0 & 0 & 0 & 0 & 0 & 1 & -1 & 1 & -1 & -1 & 1 & -1 & 1 \\ 0 & 0 & 0 & 0 & 0 & 0 & 0 & 1 & -1 & -1 & 1 & -1 & 1 & 1 & -1 \end{pmatrix}$$

APPENDIX B: STATIC CONTACT ANGLE RESULTS

To evaluate the performance of the geometric formulation in the developed model, numerically obtained contact angles are compared to the prescribed values. The deviation from the prescribed angle is calculated according to, (prescribed angle-measured angle)/prescribed angle, and the results are provided in Table II. The maximum error is ~3.7% indicating

TABLE II. Error in measured equilibrium contact angle.

Prescribed contact angle	Measured contact angle	% error
120	118.030 865 7	1.640 945 2
105	102.691 414 4	2.198 653
90	88.281 570 3	1.909 366 3
75	74.057 646 81	1.256 470 9
60	58.049 076 59	3.251 539
45	43.902 440 78	2.439 020 5
30	28.884 607 54	3.717 974 9

the current implementation can satisfactory capture solid-fluid adhesion at high density ratio.

APPENDIX C: VELOCITY PROFILES INSIDE DROP WITH AND WITHOUT SAW INTERACTION

In its current formulation, when comparing the magnitude of velocities inside the drop we cannot readily distinguish between spurious currents and acoustic streaming. As can be seen from a droplet on a surface [Fig. 20(a)], without external forcing, it displays a symmetrical pattern which is purely a consequence of the numerical scheme. Comparing it to a droplet subjected to low SAW forcing [Fig. 20(b)], we see a more asymmetric pattern, where a streaming state has been induced.

For a droplet without any SAW interaction there is a large velocity near the top center and the majority of velocities are located near the interface where interfacial tension effects are highest. On the contrary, when SAW is introduced the largest velocities are found at the left-hand side where the interaction

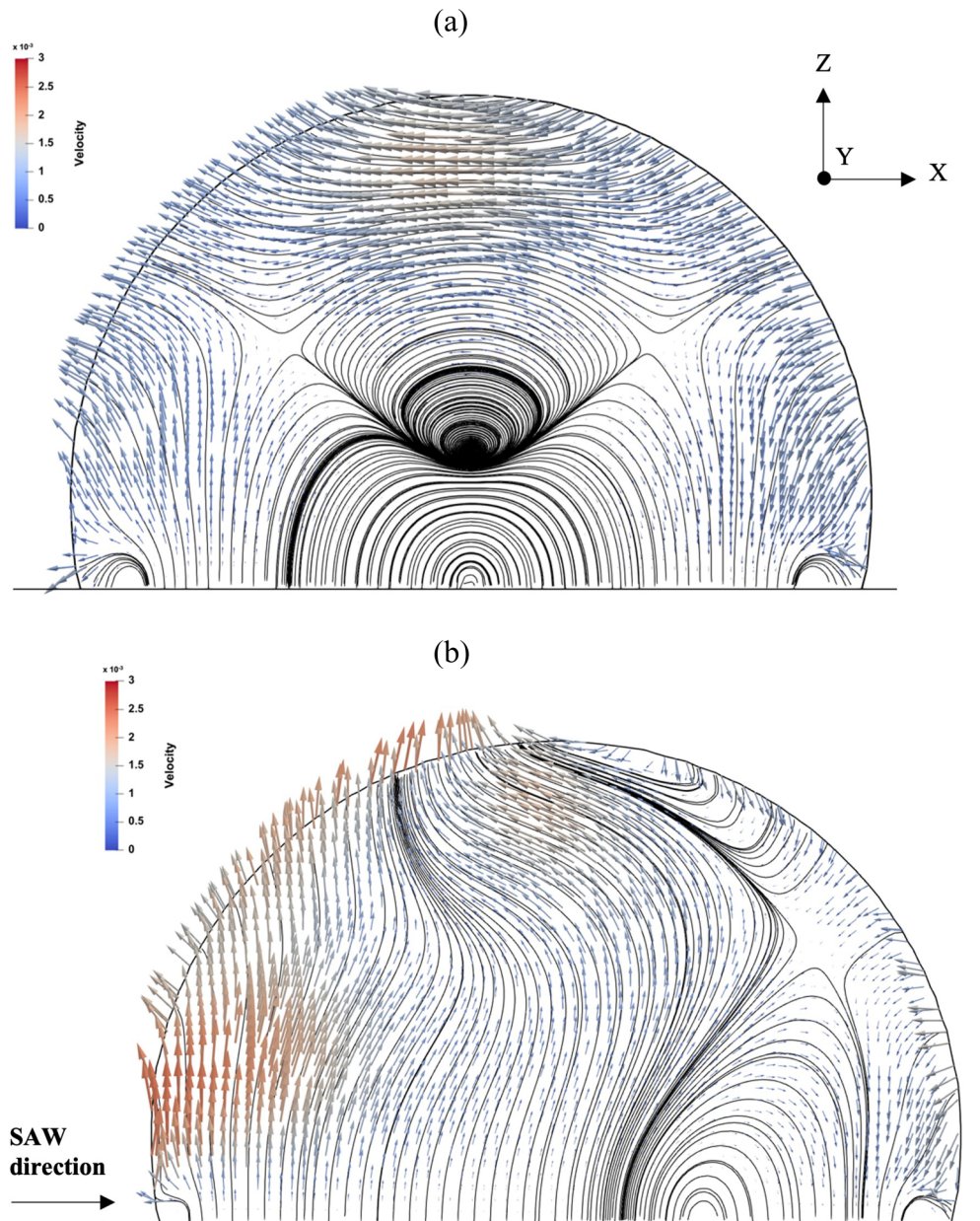


FIG. 20. Velocity streamlines and vectors for droplet with (a) no SAW interaction and (b) SAW interaction at 61.7 MHz (note: flow field in lattice units). View is slice through center of droplet at 17 ms.

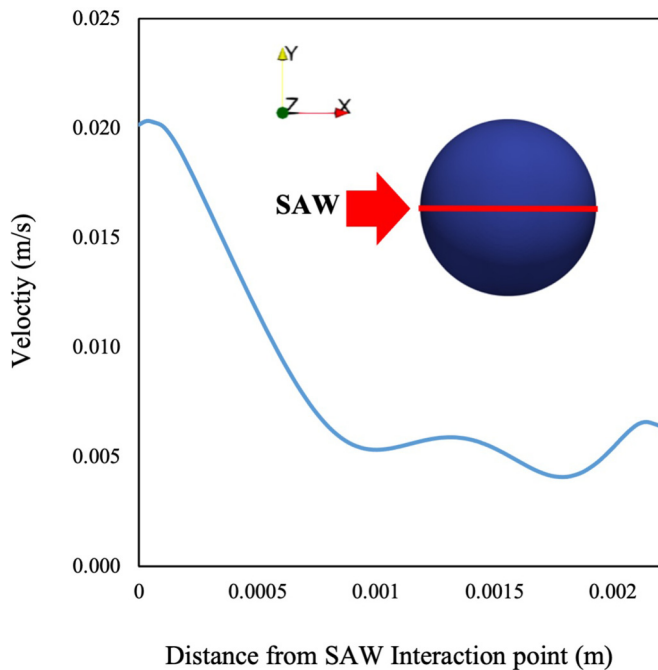


FIG. 21. Velocity profile through center of droplet ($5\text{-}\mu\text{l}$ drop at 0.4 mm above surface at 61.7 MHz).

point resides. The direction of the flow field has been altered, as the momentum of the liquid has been pushed upwards along the Rayleigh angle, with a primary vortex established at the

right-hand side of the droplet. Although the order of magnitude between the two sets of data is similar, the composition is distinctly different. When SAW is acting, a mixing field is noticeably produced.

Further indication that a streaming state is initiated is confirmed by a velocity profile across the center of the droplet. In Alghane *et al.* [11] they provide extensive details on the velocity profiles expected when a low power SAW is interacting with a $30\text{-}\mu\text{l}$ liquid droplet. They demonstrate a high velocity near the interaction area [Fig. 10(a) of [11]], diminishing along the width of the droplet with two lower peaks at the middle and far side. Now, if we look at the velocity profile across the droplet in the present study (Fig. 21), at a height of $400\text{ }\mu\text{m}$ from the droplet bottom, we see a similar outcome. Although it has already been noted that spurious velocities and streaming velocities cannot be distinguished readily, there can be no doubt that the forcing scheme employed stimulates streaming inside the drop which can cause mixing, pumping, and jetting with increase in wave amplitude (power).

The spurious currents inside the droplet can be rearranged and reorientated by the SAW forcing, as illustrated in Figs. 22 and 23, if the wave amplitude is sufficiently large. At small amplitudes it has been shown that the forcing does not add enough momentum to the fluid to alter the flow structure already imposed by the numerical scheme, hence a velocity field similar to that of a droplet without SAW interaction is achieved. This flow field is maintained with further increase in wave amplitude until it reaches a threshold, at which point the forcing is able to reorder the flow resulting in a streaming or mixing state.

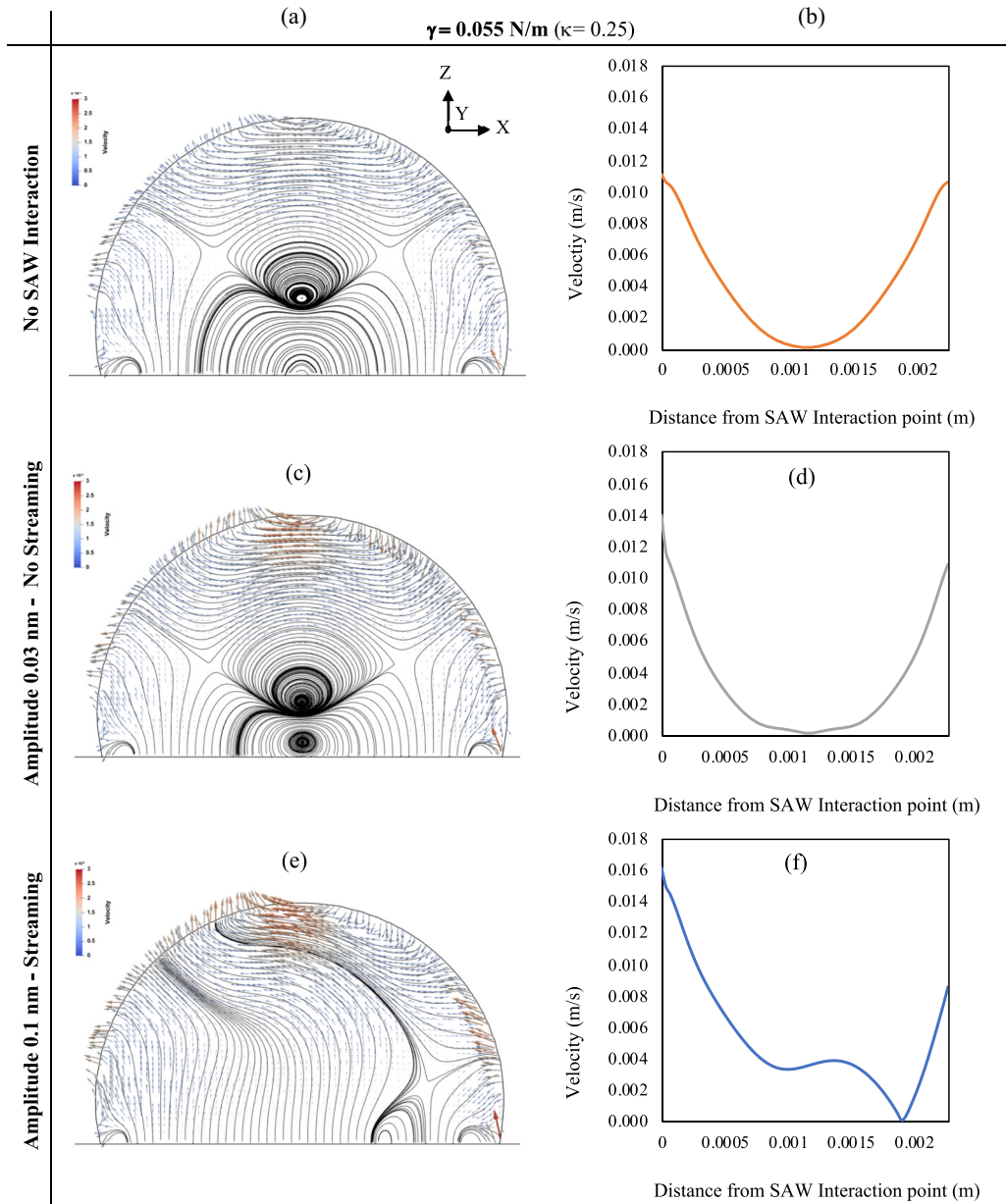


FIG. 22. Flow field and velocity profiles inside droplet at $\kappa = 0.25$ and 61.7 MHz. Droplet without SAW interaction (a),(b), and with SAW interaction; 0.03-nm wave amplitude (c),(d) and 0.1-nm wave amplitude (e),(f) (note: flow field in lattice units). View is slice through center of droplet at 17 ms.

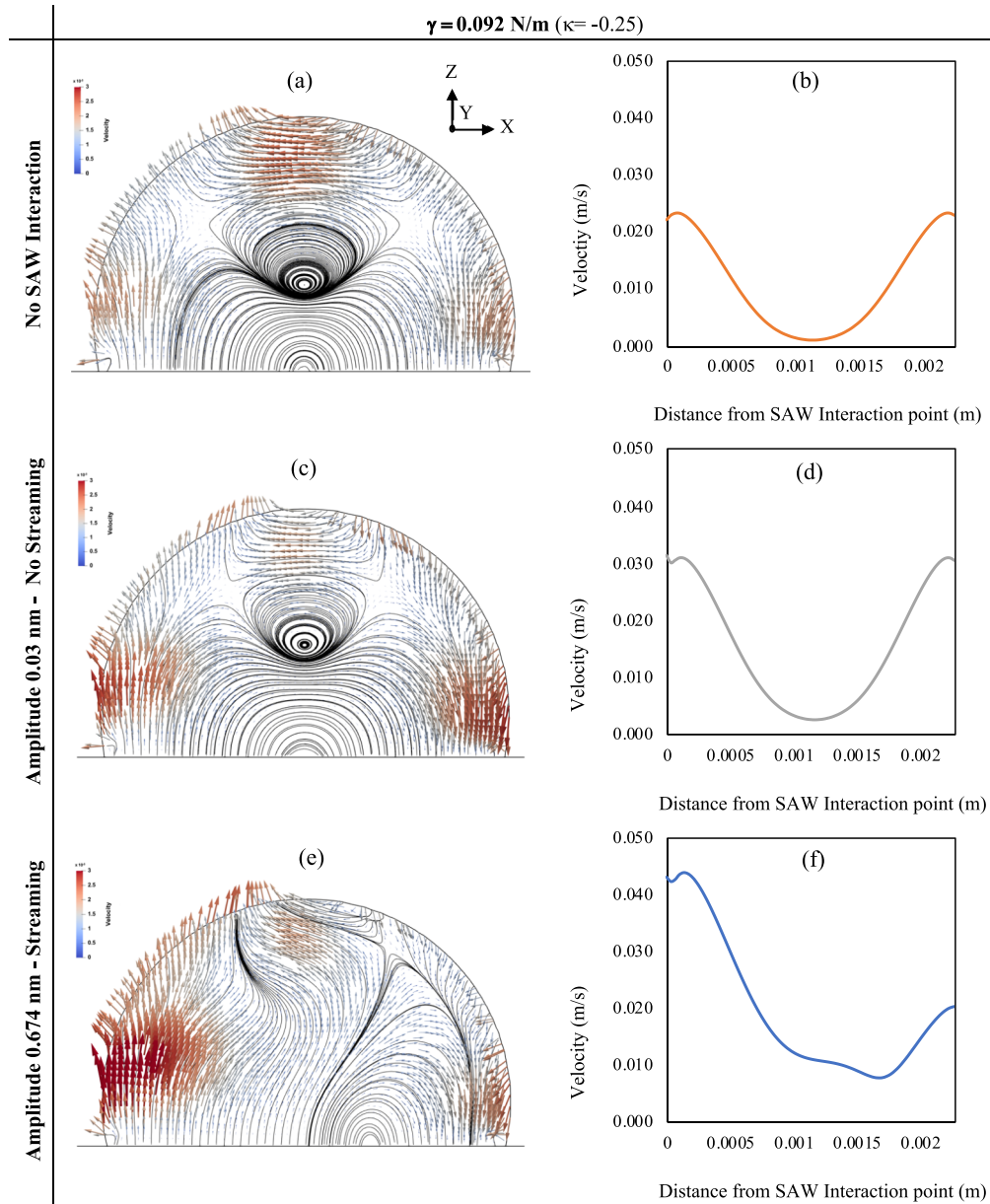


FIG. 23. Flow field and velocity profiles inside droplet at $\kappa = -0.25$ and 61.7 MHz. Droplet without SAW interaction (a),(b), and with SAW interaction; 0.03-nm wave amplitude (c),(d) and 0.167-nm wave amplitude (e),(f) (note: flow field in lattice units). View is slice through center of droplet at 17 ms.

- [1] P. Abgrall and A. M. Gué, Lab-on-chip technologies: Making a microfluidic network and coupling it into a complete microsystem - A review, *J. Micromech. Microeng.* **17**, R15 (2007).
- [2] H. A. Stone, A. D. Stroock, and A. Ajdari, Engineering flows in small devices, *Annu. Rev. Fluid Mech.* **36**, 381 (2004).
- [3] D. Mark, S. Haerberle, G. Roth, F. Von Stetten, and R. Zengerle, Microfluidic lab-on-a-chip platforms: Requirements, characteristics and applications, *Chem. Soc. Rev.* **39**, 1153 (2010).
- [4] L. Y. Yeo and J. R. Friend, Ultrafast microfluidics using surface acoustic waves, *Biomicrofluidics* **3**, 012002 (2009).
- [5] K. Sritharan, C. J. Strobl, M. F. Schneider, A. Wixforth, and Z. Guttenberg, Acoustic mixing at low Reynold's numbers, *Appl. Phys. Lett.* **88**, 054102 (2006).
- [6] R. V. Raghavan, J. R. Friend, and L. Y. Yeo, Particle concentration via acoustically driven microcentrifugation: Micropiv flow visualization and numerical modelling studies, *microfluid. Nanofluidics* **8**, 73 (2010).
- [7] J. Friend and L. Y. Yeo, Microscale acoustofluidics: microfluidics driven via acoustics and ultrasonics, *Rev. Mod. Phys.* **83**, 647 (2011).
- [8] M. K. Tan, J. R. Friend, and L. Y. Yeo, Interfacial Jetting Phenomena Induced by Focused Surface Vibrations, *Phys. Rev. Lett.* **103**, 024501 (2009).
- [9] S. K. R. S. Sankaranarayanan, S. Cular, V. R. Bhethanabotla, and B. Joseph, Flow induced by acoustic streaming on surface-acoustic-wave devices and its application in biofouling removal: A computational study and comparisons to experiment, *Phys. Rev. E* **77**, 066308 (2008).
- [10] M. Alghane, B. X. Chen, Y. Q. Fu, Y. Li, J. K. Luo, and A. J. Walton, Experimental and numerical investigation of acoustic streaming excited by using a surface acoustic wave device on a 128° YX-LiNbO₃ substrate, *J. Micromech. Microeng.* **21**, 015005 (2011).
- [11] M. Alghane, Y. Q. Fu, B. X. Chen, Y. Li, M. P. Y. Desmulliez, and A. J. Walton, Streaming phenomena in microdroplets induced by Rayleigh surface acoustic wave, *J. Appl. Phys.* **109**, 114901 (2011).
- [12] M. Alghane, B. X. Chen, Y. Q. Fu, Y. Li, M. P. Y. Desmulliez, M. I. Mohammed, and A. J. Walton, Non-linear hydrodynamic effects induced by Rayleigh surface acoustic wave in sessile droplets, *Phys. Rev. E* **86**, 056304 (2012).
- [13] A. Riaud, M. Baudoin, O. Bou Matar, J. L. Thomas, and P. Brunet, On the influence of viscosity and caustics on acoustic streaming in sessile droplets: An experimental and a numerical study with a cost-effective method, *J. Fluid Mech.* **821**, 384 (2017).
- [14] D. Köster, Numerical simulation of acoustic streaming on surface acoustic wave-driven biochips, *SIAM J. Sci. Comput.* **29**, 2352 (2007).
- [15] M. K. Tan and L. Y. Yeo, Hybrid finite-difference/lattice Boltzmann simulations of microchannel and nanochannel acoustic streaming driven by surface acoustic waves, *Phys. Rev. Fluids* **3**, 044202 (2018).
- [16] S. M. Sheikholeslam Noori, M. Taeibi Rahni, and S. A. Shams Taleghani, Numerical analysis of droplet motion over a flat plate due to surface acoustic waves, *Microgravity Sci. Technol.* **32**, 647 (2020).
- [17] M. S. Noori, A. S. Taleghani, and M. T. Rahni, Phenomenological investigation of drop manipulation using surface acoustic waves, *Microgravity Sci. Technol.* **32**, 1147 (2020).
- [18] Z. Wang and J. Zhe, Recent advances in particle and droplet manipulation for lab-on-a-chip devices based on surface acoustic waves, *Lab Chip* **11**, 1280 (2011).
- [19] A. Hospital, J. R. Goñi, M. Orozco, and J. Gelpi, Molecular dynamics simulations: Advances and applications, *Adv. Appl. Bioinforma. Chem.* **8**, 37 (2015).
- [20] P. Lallemand and L.-S. S. Luo, Theory of the lattice Boltzmann method: Dispersion, dissipation, isotropy, galilean invariance, and stability, *Phys. Rev. E* **61**, 6546 (2000).
- [21] A. K. Gunstensen, D. H. Rothman, S. S. Zaleski, and G. Zanetti, Lattice Boltzmann model of immiscible fluids, *Phys. Rev. A* **43**, 4320 (1991).
- [22] S. Saito, Y. Abe, and K. Koyama, Lattice Boltzmann modeling and simulation of liquid jet breakup, *Phys. Rev. E* **96**, 013317 (2017).
- [23] M. R. Swift, W. R. Osborn, and J. M. Yeomans, Lattice Boltzmann Simulation of Nonideal Fluids, *Phys. Rev. Lett.* **75**, 830 (1995).
- [24] T. Inamuro, T. Yokoyama, K. Tanaka, and M. Taniguchi, An improved lattice Boltzmann method for incompressible two-phase flows with large density differences, *Comput. Fluids* **137**, 55 (2016).
- [25] T. Lee and C. L. Lin, A stable discretization of the lattice Boltzmann equation for simulation of incompressible two-phase flows at high density ratio, *J. Comput. Phys.* **206**, 16 (2005).
- [26] A. Fakhari and M. H. Rahimian, Phase-field modeling by the method of lattice Boltzmann equations, *Phys. Rev. E* **81**, 036707 (2010).
- [27] S. Chen and G. D. Doolen, Lattice Boltzmann method for fluid flows, *Annu. Rev. Fluid Mech.* **30**, 329 (1998).
- [28] H. Huang, M. C. Sukop, and X.-Y. Lu, *Multiphase Lattice Boltzmann Methods: Theory and Application* (John Wiley & Sons, Chichester, UK, 2015).
- [29] Q. Li, Y. L. He, G. H. Tang, and W. Q. Tao, Improved axisymmetric lattice Boltzmann scheme, *Phys. Rev. E* **81**, 056707 (2010).
- [30] Q. Li and K. H. Luo, Achieving tunable surface tension in the pseudopotential lattice Boltzmann modeling of multiphase flows, *Phys. Rev. E* **88**, 053307 (2013).
- [31] X. Shan and H. Chen, Lattice Boltzmann model for simulating flows with multi phases and components, *Phys. Rev. E* **47**, 1815 (1993).
- [32] X. Shan and H. Chen, Simulation of nonideal gases and liquid-gas phase transitions by the lattice Boltzmann equation, *Phys. Rev. E* **49**, 2941 (1994).
- [33] A. Xu, T. S. Zhao, L. An, and L. Shi, A three-dimensional pseudo-potential-based lattice Boltzmann model for multiphase flows with large density ratio and variable surface tension, *Int. J. Heat Fluid Flow* **56**, 261 (2015).
- [34] Q. Li, K. H. Luo, and X. J. Li, Lattice Boltzmann modeling of multiphase flows at large density ratio with an improved pseudopotential model, *Phys. Rev. E* **87**, 053301 (2013).
- [35] N. S. Martys and H. Chen, Simulation of multicomponent fluids in complex three-dimensional geometries by the lattice Boltzmann method, *Phys. Rev. E* **53**, 743 (1996).

- [36] Q. Kang, D. Zhang, and S. Chen, Displacement of a two-dimensional immiscible droplet in a channel, *Phys. Fluids* **14**, 3203 (2002).
- [37] R. Benzi, L. Biferale, M. Sbragaglia, S. Succi, and F. Toschi, Mesoscopic modeling of a two-phase flow in the presence of boundaries: The contact angle, *Phys. Rev. E* **74**, 021509 (2006).
- [38] P. Raiskinmäki, A. Koponen, J. Merikoski, and J. Timonen, Spreading dynamics of three-dimensional droplets by the lattice-Boltzmann method, *Comput. Mater. Sci.* **18**, 7 (2000).
- [39] M. C. Sukop and D. Or, Lattice Boltzmann method for modeling liquid-vapor interface configurations in porous media, *Water Resour. Res.* **40**, 1 (2004).
- [40] Q. Li, K. H. Luo, Q. J. Kang, and Q. Chen, Contact angles in the pseudopotential lattice Boltzmann modeling of wetting, *Phys. Rev. E* **90**, 053301 (2014).
- [41] H. Ding and P. D. M. Spelt, Wetting condition in diffuse interface simulations of contact line motion, *Phys. Rev. E* **75**, 046708 (2007).
- [42] A. Hu, L. Li, R. Uddin, and D. Liu, Contact angle adjustment in equation-of-state-based pseudopotential model, *Phys. Rev. E* **93**, 053307 (2016).
- [43] F. Ye, Q. Di, W. Wang, F. Chen, H. Chen, and S. Hua, Comparative study of two lattice Boltzmann multiphase models for simulating wetting phenomena: implementing static contact angles based on the geometric formulation, *Appl. Math. Mech. (Eng. Ed.)* **39**, 513 (2018).
- [44] L. Wang, H. B. Huang, and X. Y. Lu, Scheme for contact angle and its hysteresis in a multiphase lattice Boltzmann method, *Phys. Rev. E* **87**, 013301 (2013).
- [45] S. Shiokawa, Y. Matsui, and T. Ueda, Liquid streaming and droplet formation caused by leaky Rayleigh waves, Liquid streaming and droplet formation caused by leaky Rayleigh waves, *Proceedings of IEEE Ultrasonics Symposium*, Vol. 1 (IEEE, Piscataway, NJ, 1989), pp. 643–646.
- [46] P. Yuan and L. Schaefer, Equations of state in a lattice Boltzmann model, *Phys. Fluids* **18**, 042101 (2006).
- [47] K. Connington and T. Lee, A review of spurious currents in the lattice Boltzmann method for multiphase flows, *J. Mech. Sci. Technol.* **26**, 3857 (2012).
- [48] X. Shan, Analysis and reduction of the spurious current in a class of multiphase lattice Boltzmann models, *Phys. Rev. E* **73**, 047701 (2006).
- [49] C. M. Pooley and K. Furtado, Eliminating spurious velocities in the free-energy lattice Boltzmann method, *Phys. Rev. E* **77**, 046702 (2008).
- [50] S. Leclaire, N. Pellerin, M. Reggio, and J.-Y. Trépanier, An approach to control the spurious currents in a multiphase lattice Boltzmann method and to improve the implementation of initial condition, *Int. J. Numer. Methods Fluids* **77**, 732 (2015).
- [51] P. G. De Gennes, Wetting: Statics and dynamics, *Rev. Mod. Phys.* **57**, 827 (1985).
- [52] M. Gross, F. Varnik, D. Raabe, and I. Steinbach, Small droplets on superhydrophobic substrates, *Phys. Rev. E* **81**, 051606 (2010).
- [53] C. A. Miller and L. E. Scriven, The oscillations of a fluid droplet immersed in another fluid, *J. Fluid Mech.* **32**, 417 (1968).
- [54] H. Lamb, *Hydrodynamics* (Cambridge University Press, Cambridge, UK, 1932).
- [55] S. Ammar, G. Pernaudeau, and J. Y. Trépanier, A multiphase three-dimensional multi-relaxation time (MRT) lattice Boltzmann model with surface tension adjustment, *J. Comput. Phys.* **343**, 73 (2017).
- [56] Y. J. Guo, H. B. Lv, Y. F. Li, X. L. He, J. Zhou, J. K. Luo, X. T. Zu, A. J. Walton, and Y. Q. Fu, High frequency microfluidic performance of LiNbO₃ and ZnO surface acoustic wave devices, *J. Appl. Phys.* **116**, 24501 (2014).
- [57] İ. Dinçer and C. Zamfirescu, Drying Phenomena, in *Theory and Applications*, 1st ed. (John Wiley & Sons, Chichester, UK, 2015), pp. 457–459.
- [58] A. E. Rajapaksa, J. J. Ho, A. Qi, R. Bischof, T. H. Nguyen, M. Tate, D. Piedrafita, M. P. McIntosh, L. Y. Yeo, E. Meeusen, R. L. Coppel, and J. R. Friend, Effective pulmonary delivery of an aerosolized plasmid DNA vaccine via surface acoustic wave nebulization, *Respir. Res.* **15**, 60 (2014).
- [59] K. Pasieczynski and B. Chen, Multipseudopotential interaction models for thermal lattice Boltzmann method simulations, *Phys. Rev. E* **102**, 013311 (2020).
- [60] R. Huang and H. Wu, Third-order analysis of pseudopotential lattice Boltzmann model for multiphase flow, *J. Comput. Phys.* **327**, 121 (2016).